

Date of publication xxxx 00, 0000, date of current version xxxx 00, 0000.

Digital Object Identifier 10.1109/ACCESS.2024.0429000

# Angle Quest: Deep Learning Approach for Tooth Segmentation and Axial Inclination Measurement in Orthopantomogram Radiographs

**ANKITHA A NAYAK<sup>1</sup>, VENUGOPALA P S<sup>2</sup> (Senior Member, IEEE), NICY THOMAS<sup>3</sup>, M.S RAVI<sup>4</sup>, and ASHWINI B<sup>5</sup> (Member, IEEE)**

<sup>1</sup>NITTE (Deemed to Be University), Department of Computer Science and Engineering, NMAM Institute of Technology (NMAMIT), Nitte, Karkala, 574110, India (e-mail: ankitu.1234@gmail.com)

<sup>2</sup>NITTE (Deemed to Be University), Department of Artificial Intelligence and Data Science, NMAM Institute of Technology (NMAMIT), Nitte, Karkala, 574110, India)

<sup>3</sup>NITTE (Deemed to Be University), Department of Orthodontics and Dentofacial Orthopedics, A.B. Shetty Memorial Institute of Dental Sciences, Mangalore, Karnataka, India

<sup>4</sup>NITTE (Deemed to Be University), Department of Orthodontics and Dentofacial Orthopedics, A.B. Shetty Memorial Institute of Dental Sciences,, Mangalore, Karnataka, India

<sup>5</sup>NITTE (Deemed to Be University), Department of Information Science and Engineering, NMAM Institute of Technology (NMAMIT), Nitte, Karkala, 574110, India

Corresponding authors: Nicy Thomas (e-mails: isnicynice@gmail.com), Venugopala P S (e-mails: venugopalaps@nitte.edu.in).

**ABSTRACT** The axial inclination of the teeth plays a significant role in orthodontics, oral surgery, and prosthodontics, ensuring the equilibrium of occlusal forces in the stomatognathic system and dental parallelism. This paper proposes a novel, automated deep learning and computer vision approach to segment and determine the mesiodistal axial inclination of individual teeth on orthopantomogram radiographs. Although the dentistry domain has explored the deep learning domain widely to solve its numerous problems, automated axial inclination and tooth morphology remain unexplored. This paper presents a customized axial inclination methodology based on deep learning and computer vision techniques that reduces time and the errors associated with manual measurements. The paper presents instance-level OPG tooth segmentation on the manually annotated dataset collected from A. B. Shetty Memorial Institute of Dental Sciences. The paper evaluates instance segmentation models using precision, recall, Dice coefficient, and IoU. The generalization of the model is justified using 5-fold cross-validation based on both object-level and pixel-level metrics. The model shows 0.83 precision, 0.92 recall, 0.87 dice coefficient, and 0.77 IoU, projecting reliable instance segmentation. Additionally, compared to existing approaches, the proposed method is reliable and faster, reducing computational overhead. The designed approach yields considerable axial inclination values, which are statistically analyzed alongside manually computed values from dentists using an unpaired t-test ( $p < 0.05$ ). The study presents a clinically relevant, reliable, scalable, and structured preserving approach that provides a strong foundation for AI-based orthodontic treatment and diagnosis.

**INDEX TERMS** Angulation, Axial Inclination, Deep Learning, Image processing, Mask R-CNN, OPG, Segmentation, U-Net

## I. INTRODUCTION

An ideal occlusion relationship is a critical factor for complete oral health. The properly aligned teeth structure and morphology play a vital role in the individual's lifestyle. A coherent tooth alignment can establish TMJ stability, harmonious facial symmetry, proper chewing, clear speech, and several benefits, ensuring a healthy lifestyle [1]. The oral dentition represents a hierarchically structured system that follows accurate angulation and alignment based on anatom-

ical rules. An accurate inter-arch relationship, defined axial inclination, and clear occlusal contacts are stated as ideal occlusion. In dental research, the distribution of occlusal force along the vertical axis of teeth is generally considered as proper axial interaction [2] [3]. In dentistry, understanding and analyzing angulation and occlusion is crucial for various dental treatments related to orthodontics, implant placement, prosthodontics, and occlusal rehabilitation. Axial inclination is a key feature that needs to be considered in orthodontic

treatment because the mesial forces, closely linked to well-defined contact points, depend on the correct axial inclination and the occlusal relationship between teeth [4].

In dentistry, treatments employ various types of diagnostic images for patient treatment and planning. Generally, intra-oral and extraoral radiographs are a basic categorization of the diagnostic images in dentistry. Today, the cone beam computed tomography (CBCT) is an advanced imaging techniques in dentistry [5] [6]. However, OPG (orthopantomogram radiograph) and panoramic imaging are widely used imaging methods with a 2-dimensional view modality. The OPGs can capture an expanded overview of the maxillary and mandibular arch with less radiation, making it suitable for imaging to diagnose jaw pathologies, bone abnormalities, impacted teeth, and many more dental surgical treatments [7] [12]. The speed, broad coverage and non-invasiveness still make OPG a widely used imaging for many dental diagnoses and examinations. Numerous research works have improved dental diagnostics through the use of OPG images. Few studies have explored the use of OPG images with deep learning models for classifying dental diseases [8]. Classical dental structures are classified and detected using web-based software [9]. The diagnosis of dental lesions and the extraction of characteristic images are performed in the research article [10]. VGG16 and InceptionV3 are applied with transfer learning-based approaches in several studies using OPG images [11].

#### A. BRIDGING CLINICAL DEMAND AND TECHNOLOGY LIMITATIONS

Axial inclination is a significant parameter in orthodontic treatment that helps design treatment, surgical ideas, and disease diagnosis. Deriving an accurate measurement is vital for root parallelism, tooth alignment, and occlusion. Currently, orthodontic dentists rely on manual and time-consuming approaches for axial inclination calculation, which are subject to human error, inter-operator variability, and time-consuming. The current practice either involves tracing paper overlays or utilizes digital cephalometric software for calculating axial inclination. Measurement time will range from 10 to 12 minutes, necessitating the dentist's complete expertise and attention. Deep learning has shown many promising applications in dentistry, such as segmentation and classification, and is less explored in the field of geometric analysis. Real-time analysis of OPG radiographs is challenging due to factors like tooth overlap, low image contrast, and the complexity of annotation. These gaps and mismatches between clinical needs and digital reality demand a promising approach for both segmentation and angulation analysis.

##### 1) An Overview of Manual Diagnostic Procedures in Clinical Dentistry

In the established approach, the axial inclination of teeth is calculated manually through anatomical tracing of OPG radiographs. Every OPG is projected onto a 5-inch by 12-inch matte acetate sheet of thickness 0.003-inch, and traced with a 0.5 mm lead pencil. Two separate dentists will work on the

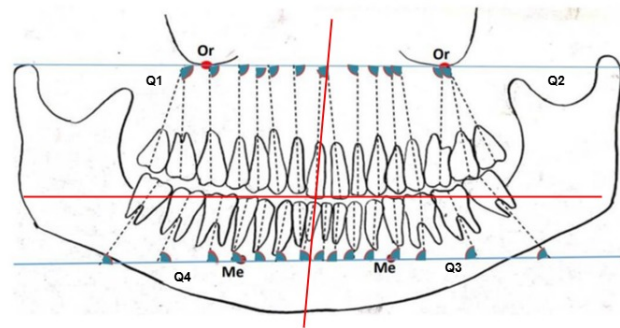


**FIGURE 1.** Landmarks and Reference Planes Outlined on OPG Radiographs for Orientation and Angulation Measurement.

same OPG to reduce intra-operator variability.

**The General OPG landmarking approach based on figure 1 is as follows:**

- 1) Orbitale (Or) — the lowest point on the inferior rim of orbit
- 2) External profile of the mandible
- 3) Mental foramen (Me)
- 4) Contours of all erupted teeth

**Reference planes used in the study based on figure 1:**

- 1) For maxillary teeth — Line joining orbitale of both sides
- 2) For mandibular teeth — Line joining center of the mental foramen on both sides

**The long axes of the teeth will be determined as described in [43]:**

- 1) Single rooted teeth — image of the root canal in its longest extent
- 2) Upper bicuspids — average image of the buccal and palatal root canals
- 3) Lower molars — average image of the mesial and distal root canals
- 4) Upper molar — image of the palatal root canal

The axial inclination angle is calculated using the upper and lower reference planes with the long axis of particular teeth. To obtain further angulation, the maxillary teeth and mandibular teeth are separated by a horizontal line. And vertical division is achieved by drawing a vertical line between the maxillary central incisors and mandibular central incisors. In the four achieved quadrants, the angle of each internal angle towards the vertical division line is recorded. The identified landmark is shown in Figure 1.

This paper presents an automated segmentation and axial inclination calculation of individual teeth using a deep learning and computer vision approach using OPG radiographs. The designed novel deep learning methodology overcomes the drawbacks of existing techniques, reducing human intervention and setting a standard for AI diagnosis in the field of orthodontics.

#### B. CONTRIBUTION

The key contributions of this research paper are listed below.

- 1) The paper proposes a novel, fully automated end-to-end framework for directly estimating individual tooth axial angulation using OPG radiographs, effectively replacing traditional manual and semi-automated measurement workflows.
- 2) A robust deep learning instance segmentation framework is applied using comparative experimental evaluation, enabling accurate individual tooth segmentation in OPG radiographs with reliable geometric analysis.
- 3) A domain-specific, geometric post-processing approach is developed to automatically derive individual tooth midpoints, generate a vertical reference axis, and compute Mesiodistal axial inclination for each tooth with minimal human intervention.
- 4) A comparative experimental study is proposed to analyze the effect of data augmentation on OPG-based tooth segmentation.
- 5) A custom OPG dataset is created for multiple segmentation with split masking, COCO JSON format, and augmented data.
- 6) The developed model performance is rigorously tested through quantitative and qualitative analysis in collaboration with clinical experts, ensuring reliability and suitability for clinical application in automated axial angle calculation.
- 7) The developed model demonstrates effective operation with limited GPU resources.

This article presents a systematic approach to demonstrate the proposed automated measurement of axial inclination using AI. Section I of the paper presents a comprehensive introduction to OPG radiographs, emphasising occlusion and axial inclination. Additionally, the existing clinical manual approach for calculating axial inclination and the contributions of the paper are outlined. Section II reviews the existing works based on well-defined research questions, highlighting research gaps identified for the proposed methodology. Section III illustrates a well-structured methodology for segmentation and axial inclination calculation, with a detailed and defined data flow from preprocessing to final statistical analysis. Section IV delivers the results of instance segmentation along with generalization and error analysis. This section offers quantitative and statistical analysis of the outcome, demonstrating the clinical feasibility of the proposed model. Section V concludes the paper with the key findings and limitations of the paper, highlighting the focus on potential future enhancements.

## II. LITERATURE REVIEW

Nowadays, numerous articles are published by researchers in the domain of dentistry, integrating with the AI arena. The dentistry domain has seen a vast and rapid growth in the application of AI models. To conduct a literature survey for this paper, selecting, managing, and consolidating existing research articles across various domains is a challenging task. In this paper, a well-defined set of questions is framed under the supervision of experts to execute a detailed literature survey

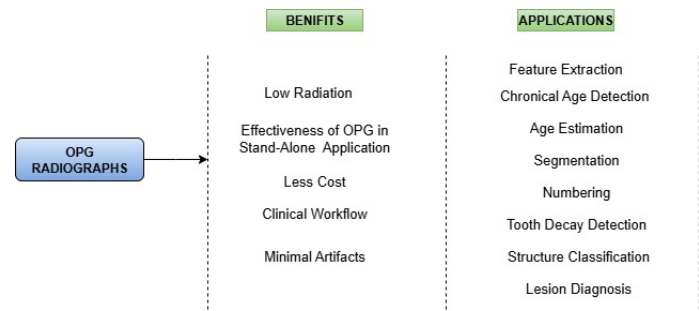


**FIGURE 2.** Overview of Benefits and Applications of OPG Radiographs in Dental Practice.

that supports segmentation, angulation, and the feasibility of OPG image in axial inclination calculation. Table 1 outlines the key research questions structured for this current study.

**TABLE 1.** Structured Research Questions

Structured Research Questions
1. Why are OPG radiographs considered in many orthodontic diagnoses?
2. What are the existing digital tools in assistance of AI available for clinical measurement analysis in dentistry?
3. How are AI techniques applied for OPG segmentation and landmark detection using OPG images?
4. What are the core issues still overlooked in OPG analysis techniques?
5. What are the current existing applications of OPG radiographs for mesiodistal axial inclination calculation?

## A. WHY ARE OPG RADIOPHGRAPHS CONSIDERED IN MANY ORTHODONTIC DIAGNOSES?

In current dentistry, OPG radiographs, also known as panoramic radiographs, are the most widely used imaging modality compared to CBCT and others. OPG is an affordable imaging technique that projects maximum tooth structural information, namely tooth number, morphology of the tooth, crown, root, mesiodistal axial inclination, eruption sequence, and spatial relation. It also provides the entire mandibular arch and maxillary arch, including TMJ and other structures [13]. OPG radiographs are widely accepted imaging compared to advanced imaging techniques due to their cost, radiation safety, patient comfort, and other traditional practices [14].

The outcome of OPG radiography is enhanced in terms of quality, minimal inter-observer variability, and cost efficiency. The outcome analysis of OPG radiographs in various disease diagnoses using CNNs and deep learning has shown remarkable progress in automated segmentation of teeth [15], [17], [18], [19], [20], caries detection, tooth decay detection [21], anomaly tooth eruption, and chronological age estimation [16], [27]. In the methodology of structural classification [22], distance and angle measurement [23], OPG radiographs are widely accepted. In [13], it is proved that OPG and CBCT radiographs provide similar angulation values during analysis with a lower error rate. The simple analysis of the advantage and applications of using OPG radiograph is given in Figure 2.

### B. WHAT ARE THE EXISTING DIGITAL TOOLS IN ASSISTANCE OF AI ARE AVAILABLE FOR CLINICAL MEASUREMENT ANALYSIS IN DENTISTRY?

In [23], evaluation of the automated dental setup software systems is performed in terms of accuracy and efficiency. Autolign, Ortho Simulational, and Orthocean Software Pro are among the software considered for testing. The selected automated software was well compared and evaluated with the manual setup of Maestro 3D Dental Studio Software. The analysis reveals software model efficiency in deriving occlusion indices. The software still demands human intervention in clear aligner therapy and indirect bonding. The root inclination of anterior teeth is estimated in [24]. The study utilizes high-resolution scanning software such as Ortho Insight 3D scanners and Motion View LLC version 4.0.6. The study estimates a small error margin between the software-based and manual approaches. However, the study is limited to only crown roots. Overlapping roots of adjacent teeth still need manual intervention. In [25], a reliability and validity study is presented on AI-based software CephX. The software program integrates a specific segmentation tool model with an intraoral scan. The pretreatment intraoral scan and CBCT scan are used for the validation test. The dataset was acquired from 10 patients with a malocclusion Class I Case. The analysis demonstrates similar accuracy on 3D segmentation aspects. The study concludes that AI software is reliable only in mild crowding scenarios and for no teeth restoration.

### C. HOW ARE AI TECHNIQUES APPLIED FOR OPG SEGMENTATION AND LANDMARK DETECTION USING OPG IMAGES?

Currently, the application of AI models in dentistry has become a trending topic among researchers. Various AI models are used to overcome the limitations of the manual approach in existing methods. Techniques such as segmentation, tooth numbering, cavity detection, root canal, malocclusion detection, and gingival invasion calculations have seen extensive adoption of deep learning and CNN models. Between 1988 and 2024, dentistry has seen a progressive growth of AI using OPG radiographs [26] [31]. In the article by Wu Chen et al. [32], a brief survey was conducted to visualize the progress of Artificial Intelligence in dentistry. It is concluded that the introduction of AI in clinical dentistry shows accurate results. Hanan Ahmed Assiri et al [27]. present a brief overview to understand the specification and usage of AI for third mandibular molar impaction.

In [28], segmentation, automatic segmentation of periapical lesions is performed using OPG radiography. The model shows a promising precision of 0.82. In [15], an OPG dataset is presented that is suitable for ML and AI algorithms in segmenting and tooth numbering tasks. The primary features of the dataset are dual annotation, which facilitates both class-wise and number-based segmentation. In [29], the Mask R-CNN is used for dental OPG segmentation. They created a dental database with a batch size of 10 and achieved an accuracy of 88.1% for teeth classification. In a recent arti-

cle by [18], the segmentation of teeth using an OPG image is performed using a U-Net architecture. In this paper, the six variants of the U-Net model were enhanced using Dice Coefficient, F1 score, and IoU evaluation ratio. The vanilla U-Net demonstrated the highest accuracy of 95.6% while the 3-layer dense U-Net gave an accuracy of 95.94%. In some research works, third molar eruption and molar angulation are calculated using an AI-based approach. The article performs customized segmentation of mandibular molars using OPG radiographs. The approach employs a fully CNN with a ResNet 101 backbone with an IoU of 90% [30]. In several research articles, a comparative analysis is performed for dental age estimation in adults using OPG and a CNN model. The evaluation metrics, such as accuracy and MAE, are used to achieve better outcomes in contrast enhancement and region segmentation. In [33], a clinical tool is designed with the support of AI and YOLOv11 sub models, to evaluate problems in the extraction of mandibular third molars. The YOLOv11 sub-model is trained using three basic scenarios: Pederson index criteria, angulation, and Peel and Gregory. The model showed high accuracy in all the scenarios. The tabular analysis of the literature survey is illustrated in Table 2.

### D. WHAT ARE THE CORE ISSUES STILL OVERLOOKED IN OPG ANALYSIS TECHNIQUES?

Despite huge advancements in dentistry and automated radiograph analysis, few challenges and limitations remained unaddressed. According to the literature survey, the major works in OPG radiograph analysis are connected to pure dentistry. Dentistry in association with AI is an evolving research area where the research articles are limited. The collected research articles in dentistry in association with AI are mainly focused on segmentation and numbering. A few notable works are studies of dental cavity, occlusion, and lesion detection. A countable work presents on measuring axial inclination angle, primarily focusing on molars or incisors. In the existing survey section, no research article has computed the angulation of each tooth in the OPG radiographs. The segmentation of teeth is still a challenging research problem due to their complex and crucial structure. The precise localization of landmarks is still a complex area to address. In addition, poor generalization and a scarcity of clinically validated algorithms to adopt in real-world practice. These drawbacks and gaps demand the need for robust and clinically oriented OPG analysis frameworks.

### E. WHAT ARE THE CURRENT EXISTING APPLICATIONS OF OPG RADIOGRAPHS FOR MESIODISTAL AXIAL INCLINATION CALCULATION?

The axial inclination of teeth is generally categorized as mesiodesital and buccolingual inclination. This article mainly presents the automated calculation of the mesiodistal axial inclination of teeth. To analyse the suitability of the OPG radiograph, this subsection reviews numerous articles that demonstrate mesiodental axial inclination using OPG radio-

**TABLE 2. Summary of Related Work**

Author	Objective	Data Type	Outcome	Dataset
Hyein Woo et al. [23]	Computation analysis of system Software with manual setup	Maestro 3D Dental Studio 3D imaging	Human intervention required in clear aligner therapy	digital impression data: 330 patients
Mehmet Boztuna et al. [28]	periapical lesions segmentation	OPG Radiographs	Promising results with 0.82 precision, 0.77 recall	400 OPG(private clinical images)
Giulia Rubiu et al. [29]	Tooth segmentation using Mask R-CNN	OPG	Performance Accuracy 98.4% and Dice Index 0.87	Tufts dataset
Rafiatul Zannanh et al. [18]	Semantic tooth segmentation using U-net	OPG	Accuracy for dense u-Net 95.56%	384 OPG (private dataset)
Myrthel Vranckx et al. [30]	Molar angulation calculation	OPG	IoU 90%, accuracy 77.7%	838 OPG radiographs (private dataset)
Serap Akdogan et al. [33]	Assessing difficulty in mandibular third molar tooth extraction	OPG	System was successful in determining positional relationship, precision 97%, recall 94.55%	571 OPG radiographs (private dataset)
Eunhye Choi et al. [34]	positioning of third mandibular molar and IAN in OPG radiographs using AI	OPG	superior ResNet-50 architecture	571 OPG radiographs(Private dataset)
Javier Pérez de Frutos et al. [35]	Application of deep learning in proximal caries	bitewings database	ResNet and YoloV5 will increase F1 score and accuracy	From the HUNT4 Oral Health Study-13,887 bitewings dataset
Wanting Qu et al. [36]	Mandibular symmetry identification and assessment	OPG	82.52% and 75.24% accuracy in diagnosis	1038 OPG Radiographs(Private Dataset)
Niha Adnan BDS et al. [37]	Segmentation of teeth and periapical lesions on pantomographs using multi-modal deep learning Method	pantomographs	U-net periapical model give precision is 84.5% and re-call is 80.3%, Mask R-CNN model gives outcome of precision of 80.6% and recall of 55%	250 pantomographs (Private dataset)
Thorbjørn Louring Koch et al. [38]	Segementation of Dental Panoramic Radiographs with U-NETS	dental panoramic radiographs	FCN with U-Net with Dice score of 0.934	1500 dental panoramic radiographs
Dmitry V Tuzoff et al. [39]	panoramic radiographs tooth detection and numbering using Convolutional neural network	panoramic radiographs	Faster R-CNN architecture and VGG-16 CNN model with precision of 0.9945 for teeth detection	1352 panoramic radiographs
Fahad Umer et al. [40]	Comparision of DL models for teeth Detection	panoramic radiographs	Faster R-CNN achieved higher precision of 0.99	1500 radiographs
Gil Jader et al. [41]	Instance Segmentation of Teeth using Panoramic X-Ray Images	Panoramic X-Ray Images	Mask R-CNN using with precision 94% and recall of 84%	1500 Panoramic X-Ray Images
Chisako Muramatsu et al. [42]	automatic dental chart filing using AI	panoramic radiographs	sensitivity for tooth detection 96.4% with 0.5 false positives per case	100 panoramic radiographs (Private Dataset)

graphs. In Orhan Cicek et al. [44], a comparative study is presented on mesiodistal axial angulation measurement of first molar and canine teeth from pre- and post-treatment panoramic radiographs. A total of 237 female and 115 male OPG radiographs were considered for the retrospective study. The measurement was calculated using the IC measure on canines, and a statistical study was conducted using the sample t-test and the Wilcoxon test. In Daniel G Bouwens et al. [45], a comparative study on mesiodistal root angulation is performed using panoramic radiographs and CBCT radiographs. It is concluded that the statistical analysis ( $p < 0.001$ ) is considered significant, as there is no difference

between OPG and CBCT images. In Caroline Andrade Rocha et al. [46], the maxillary molar mesiodistal axial inclination is calculated using an OPG radiograph. The long-term stability of mesiodistal axial inclination generated by the pendulum appliance is analysed. In Utsav Gautam et al. [47], mesiodistal angulation is carried out on mandibular canines and posterior teeth using OPG with or without a third molar. The study employed a 66-OPT and t-test approach for measurement. In Ananya Hazare et al. [48], mesiodistal angulation of maxillary first and second premolars, and the first and second molars, is calculated in reference to the infraorbital and Bi-Gonial plane in OPG radiography. In the article by Faisal M

Ansari et al. [49], the author demonstrates that OPG can be used to calculate the canine axial inclination, and no significant difference in the outcome is observed while using OPG. In Taha Zirek et al. [50], the study presents the localization of impacted teeth and winter angulation for OPG radiograph using YoloV8.

Further, Orhan Cicek et al. [51], analyses post treatment changes in mesiodistal axial angulation of central incisors and maxillary canines for the MBMLI study. The study incorporates 56 patient OPGs analyzed with SPSS version 26. Several articles, such as Renata Rodrigues de Almeida-Pedrin et al. [52], used panoramic radiographs to calculate the mesiodistal axial inclination of maxillary anterior teeth. In the article S S Samawi et al. [53], published in 1984, OPG radiography was employed for angle distortion calculation. In 2003, Poonam Agarwal et al. [54], presented a paper on the assessment of mesiodistal angulation using OPG radiographs. The paper presented a 99% confidence interval and concluded that OPG radiography can be used in mesiodistal angulation. The study was done manually using acetate paper.

### III. METHODOLOGY

This section outlines the detailed exploration of the methodology used to automate and quantify the tooth segmentation in OPG radiographs using an Artificial Intelligence-based approach. Subsequently, the paper presents the justification for choosing the current approach over the existing baseline methodology. The dataset plays a significant role in most of the studies related to AI. An overview of dataset acquisition, collection, and preparation is highlighted in the study. A detailed architecture of the proposed methodology is explained, along with an explanation and analytical justification for the individual module.

#### A. WHY IS MASK R-CNN CHOSEN OVER A WELL-KNOWN U-NET MODEL FOR SEGMENTATION?

OPG radiographs are medical imaging that possesses complex anatomical structures, occlusion, panoramic distortion, low contrast in soft tissue, and minimal space overlapping, which hinders the performance of traditional segmentation models. Generally, segmentation is classified into two types: semantic and instance level. Semantic level segmentation is a computer vision approach in which each pixel is assigned a class label. Each OPG image assigns value 1 to a tooth pixel and 0 to the background. The primary objective of OPG semantic level segmentation is to classify the teeth pixels versus background pixels. The U-Net model is one of the prominent semantic approaches in medical applications. Based on the literature review recommendation, this study executes the U-Net model to achieve the segmentation of OPG radiographs. The basic U-Net model was executed on Google Colab T4 GPU using 110 OPG radiographs for segmentation.

In the first case, the model was trained for 60 epochs with an approximate execution time of 2 hour and 45 minutes, resulting in unclear segmentation. In the second case, the model was trained for 90 and 130 epochs with an approximate

execution time of 5 hours and 15 minutes and 8 hours and 50 minutes; however, the segmentation remained unclear where adjacent tooth roots overlapped. The segmentation executed is shown in Figure 3 and blue lines represents detected boundaries.

Based on the outcome of U-Net, it is concluded that semantic segmentation requires a larger number of epochs, resources, and execution time. The segmentations fail in cases such as adjacent tooth root overlapping, complex occlusion, contour detection, and poor OPG contrast. Moreover, the U-Net didn't give the expected outcome in individual teeth separation.

Highlighting the challenges of semantic segmentation in OPG radiographs, this paper aims to segment each tooth using the Mask R-CNN model. The Mask R-CNN model extends Faster R-CNN with parallel pixel-wise segmentation. Mask R-CNN is an instance segmentation with the potential to handle complex boundaries and tooth-wise anatomical analysis. Hence, this paper implements Mask R-CNN for the further segmentation process.

#### B. STUDY FRAMEWORK

This section presents the overall research flow of the designed methodology, with a detailed visual representation in Figure 4. The proposed approach follows a structured pipeline approach from data collection to quantitative validation.

Initially, a patient will undergo panoramic imaging technique under the supervision of a dentist in a controlled clinical environment utilizing standard imaging protocols. The acquired OPG radiographs proceed with clinical annotation in two approaches: manual and digital. The manual annotation traces the boundaries of the teeth and the reference line on the trace by an expert dentist. The digital annotation utilizes the LabelMe tool with oversight from technical and dental experts. Notably, the manual annotation value serves as a reference for the further validation process.

The acquired OPG radiographs follow preprocessing approaches, including resizing and contrast enhancement. The dataset augmentation techniques, such as Horizontal Flip, Vertical Flip, Rotation (typically  $\pm 90^\circ$ ,  $180^\circ$ , or random angles), Brightness Adjustment, Contrast Adjustment, and rescaling, are performed to increase the cohort size. The annotated data was converted to the COCO dataset format, enabling compatibility with Mask R-CNN segmentation. The original OPG radiographs, along with the generated labels, are cascaded to the segmentation module.

The segmented radiographs proceed to the axial inclination measurement module, which comprises a custom-designed sub-module involving midpoint detection, vertical line generation, horizontal reference line marking, intersection of vertical and horizontal reference lines, and calculation of the angle between intersection points. Finally, the digitally calculated axial inclination angle is verified with the manually calculated angle using the Shapiro-Wilk test for normality and Levene's test for homogeneity of variance using SPSS version 23.

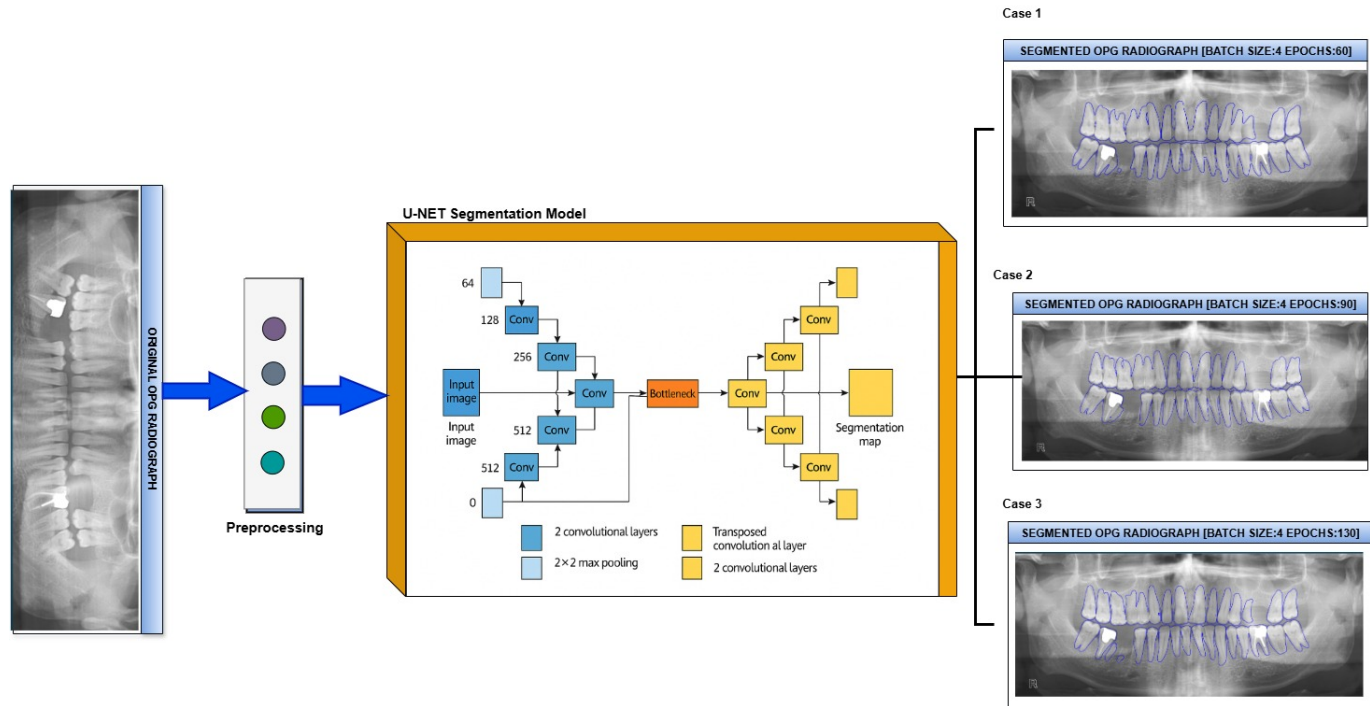


**FIGURE 3.** The Outcome of U-Net Segmentation Model across Different Training Epochs: Case 1 – 60 epochs, Case 2 – 90 epochs, and Case 3 – 130 epochs.

#### C. DATA COLLECTION

Before training the model, data collection and preprocessing are the essential steps to ensure better performance, clarity, and a standard dataset. In this study, orthopantomogram radiographs were retrospectively collected from patient records at the Department of Orthodontics and Dentofacial Orthopedics, A. B. Shetty Memorial Institute of Dental Sciences (ABSMIDS), Mangalore, India, in compliance with ethical guidelines and standard clinical imaging protocols. The collected dataset was de-identified and delinked to maintain patient privacy. Additionally, this study receives ethical clearance from the Institutional Ethics Committee. Furthermore, the collected data undergo a filtering method with specific inclusion and exclusion criteria to ensure a standard and suitable dataset. The sample images of the collected dataset is shown in Figure 5.

The designed Inclusion Criteria for the study are as follows:

- 1) Patient age range: 18 to 30 years.
- 2) The standard and high-quality OPG radiographs. from the patients who underwent routine orthodontic treatment.
- 3) The OPG radiographs of patients who were willing to participate in the study and gave informed consent.

The drafted exclusion criteria for the study are as follows:

- 1) OPGs with severe noise, distortion, positional errors, or imaging artifacts.
- 2) OPG radiographs with imaging artifacts, more noise, positioning error, and distortion.
- 3) OPG radiographs with dilacerated or Unerupted teeth.

- 4) Teeth with coronal restorations were affected in both coronal shape and size.
- 5) OPG radiograph with root resorption teeth and gross dental caries
- 6) OPG radiographs with bone disorders, systemic illnesses, chronic periodontal disease, and craniofacial abnormalities.

#### 1) Justification for Sample Size Calculation

During dataset preparation, the required sample size analysis is calculated through a statistical formula based on a binomial-based reliability validation model. The statistical formula is given in equation (1).

$$n = 1 + \frac{2(z_\alpha + z_{1-\beta})^2}{(\ln C_0)^2(k-1)} k \quad (1)$$

where

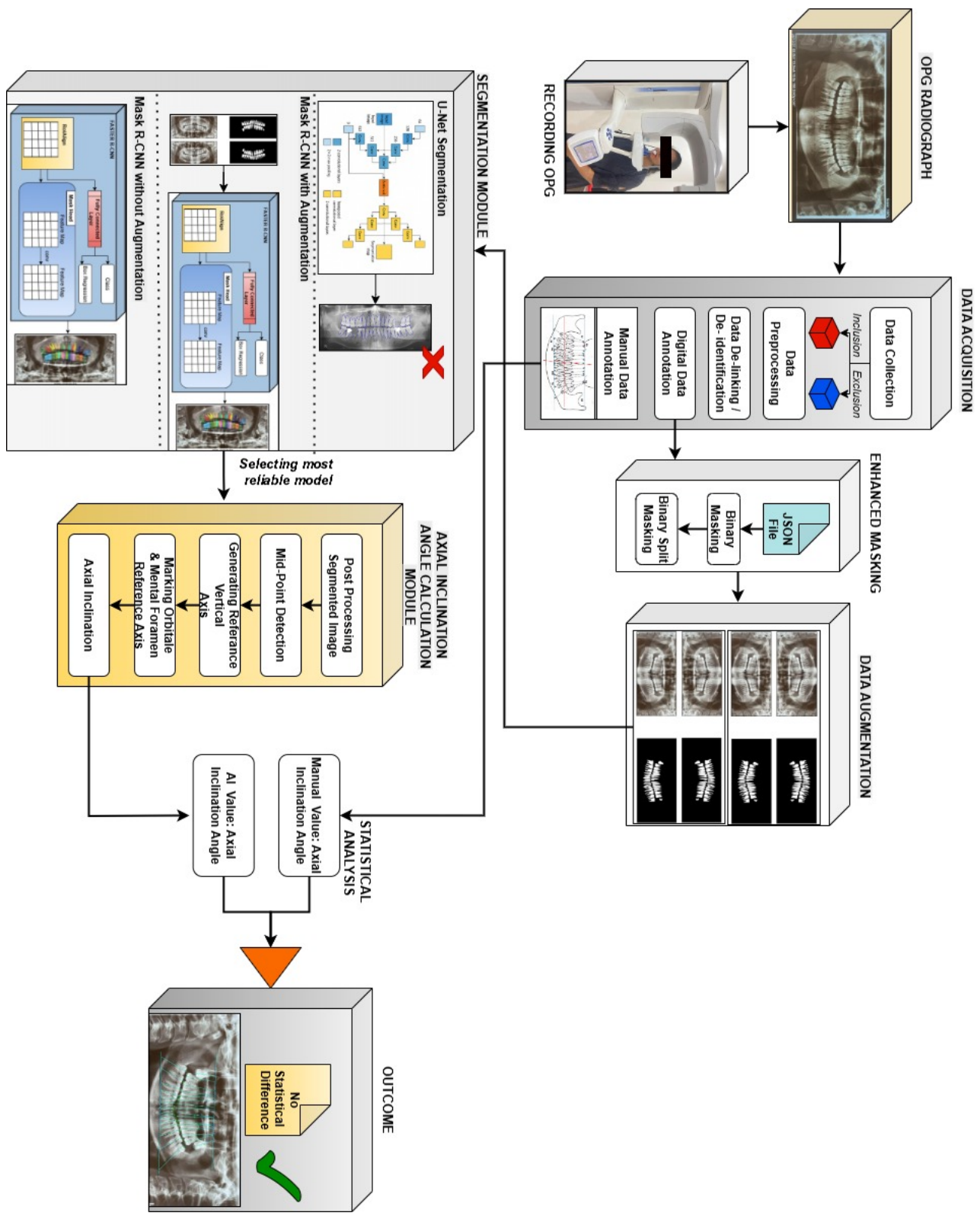
$$C_0 = \frac{1+k\theta_0}{1+k\theta} \quad \theta_0 = \frac{\rho_0}{1-\rho_0} \quad \theta = \frac{\rho_1}{1-\rho_1}$$

with the parameters:

- $\rho_0$  : Sample reliability value
- $\rho_1$  : Population reliability value
- $k$  : Number of replicates
- $\alpha$  : Significance level
- $1 - \beta$  : Power

In this experiment, the sample reliability value ( $\rho_0$ ) is assigned as 0.9799, ensuring the reliability of the collected data. The target population  $\rho_1$  is given as 0.99, representing the required threshold for generalizability. The power was

**FIGURE 4.** Architecture of the Proposed Novel Framework comprising Data Acquisition, Mask Enhancement, Data Augmentation, Segmentation, Angulation, and Statistical Analysis Modules.



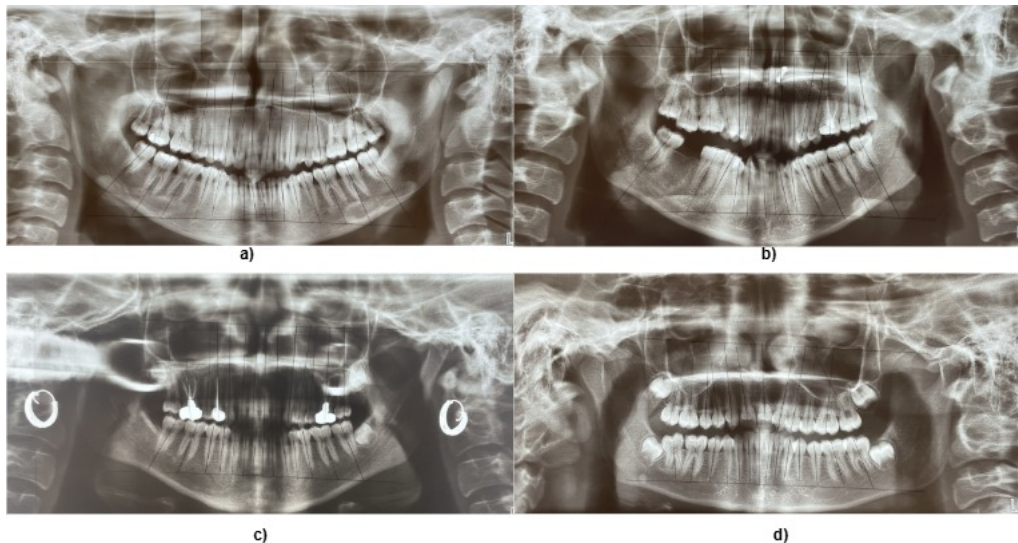


**FIGURE 5.** Sample Images of Collected OPG Radiograph Dataset: a) Normal Standard OPG b) Missing Tooth OPG c) Low Contrast OPG d) Unerupted Teeth OPG

initialized to 95% and the alpha error of 5%. The number of replicates is 2. Finally, the formula calculates that the required dataset should be 110 OPG radiographs. The derived sample size affirms that the model trained delivers a high probability of true positives by reducing false positives.

#### D. DATA PROCESSING AND SYNTHESIS

After collecting the data of the required sample size, the next step includes data preprocessing. In the devised methodology, the basic preprocessing functions, such as resizing and contrast enhancement, are applied. The resizing technique is applied to obtain an image suitable for the segmentation model, and contrast enhancement is used to preserve and improve the visual clarity of the OPG. In this research work, to analyze the existing well-known segmentation algorithms to choose an appropriate one, two types of segmentation are experimented with. To support each segmentation model, two types of annotations are executed.

##### 1) Annotation Using LabelMe Tool

Each preprocessed OPG images are imported into the LabelMe tool for further annotation. Initially, the overall annotation approach is performed under the guidance of dental experts possessing rich experience in analysing OPG radiographs. To ensure consistency and avoid inter-operator variability, the dataset subset was independently annotated by multiple dental experts. The complete annotation follows the standard quality protocol with regular review and validation of subsets to ensure the high fidelity and reliability of the annotation process. In the LabelMe annotation, the polygon selection tool is used to annotate individual teeth. This annotation supports semantic-level U-Net Segmentation. The LabelMe annotated mask is shown in Figure 6.

##### 2) Refining Overlapping Masks with Split-Based Manual Annotation

In the LabelMe annotation, it is observed that adjacent teeth that are closely connected or have close roots are not efficiently segmented in binary mask generation. This issue arises due to the continuity of the inherent anatomy in OPG radiographs, causing a merged mask with negligible inter-tooth separation.

During the annotation process using the LabelMe tool, it was observed that adjacent teeth—especially those with overlapping or closely approximated roots—were not adequately segmented in the generated binary masks. This issue predominantly occurred due to the inherent anatomical continuity in OPG radiographs, leading to merged masks in regions with minimal inter-tooth separation.

To overcome this limitation, a manual optimized approach is implemented. A split-mask approach is introduced, where boundaries of closely connected teeth are manually defined with clear visible contours. This manual mask refinement approach is named split masking to achieve a better ground truth by clearly differentiating connected contours. This optimized annotation approach overcomes the bottleneck of segmentation models in the challenging, crowded root region. The approach possesses the ability to enhance overall segmentation quality by handling the ambiguity of adjacent tooth boundaries. The split mask image is illustrated in Figure 6.

##### 3) Data Augmentation for Robustness

To increase the generalization potential and diversity of the segmentation model, the original acquired dataset of sample size 110 OPG radiographs is elaborated using a structured augmentation process. In this approach, each image is augmented using two different techniques from Table 3. The augmentation process executes in a controlled manner where every image chooses any two distinct transformations, with

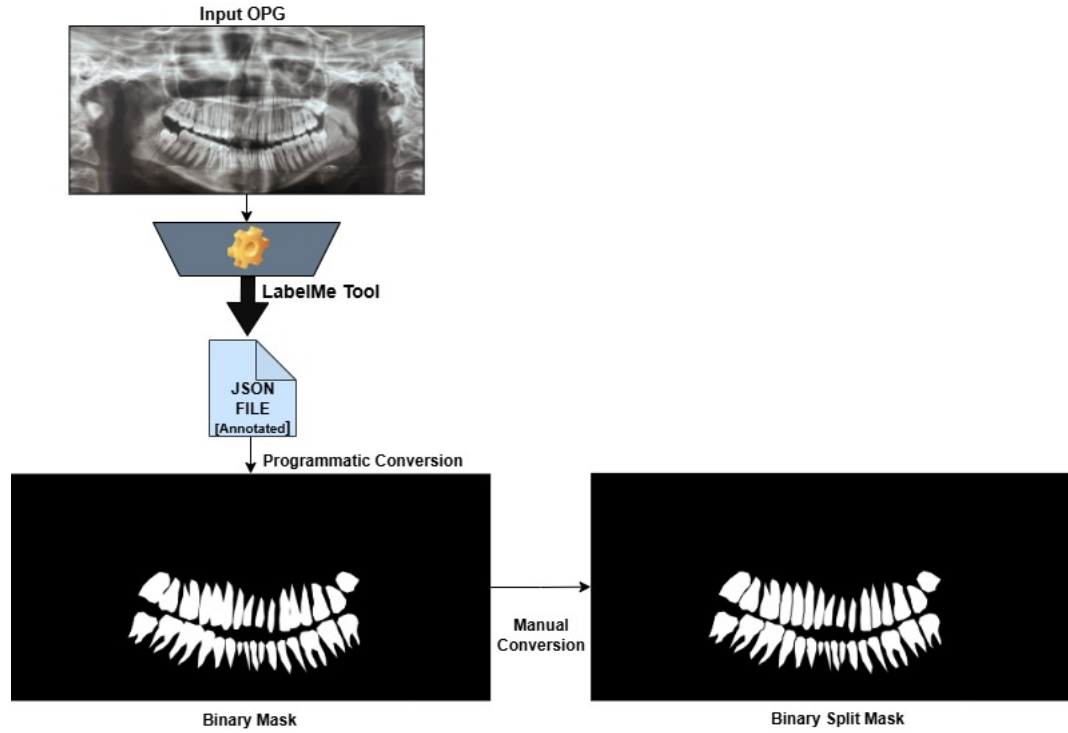


**FIGURE 6.** Mask Generation Process Comprising the LabelMe Annotation Tool and Manual Split-Mask Refinement.

**TABLE 3.** Standard Transformation Methods for OPG Data Augmentation

Conventional Transformation Method
Horizontal Flip
Vertical Flip
Rotation (within $\pm 15^\circ$ )
Brightness and Contrast Adjustment
Gaussian Blur

no two augmented copies having the same transformation. The overall outcome of this approach is 220 images, which are combined with the original images. The detailed algorithm is shown in Algorithm 1. A simple mathematical formulation proof is as follows: Assume the original dataset of OPG radiographs is:

$$\mathcal{OD} = \{OD_1, OD_2, \dots, OD_{110}\} \quad (2)$$

where dataset total value will be  $|\mathcal{OD}| = 110$ . The  $\mathcal{OD}$  is original OPG radiograph. The considered augmentation transformations for the augmentation are:

$$TA = \{TA_1, TA_2, TA_3, TA_4, TA_5\} \quad (3)$$

where:

- $TA_1$  = Horizontal Flip
- $TA_2$  = Vertical Flip
- $TA_3$  = Rotation by  $\pm 15^\circ$
- $TA_4$  = Brightness/Contrast Adjustment
- $TA_5$  = Gaussian Blur

For every image  $I_i \in \mathcal{OD}$ , exactly 2 distinct transformations are considered from  $\mathcal{TA}$ . The subset considered will be:

$$\mathcal{A}_i = \{TA_{i1}, TA_{i2}\} \subset \mathcal{TA}, \quad \text{with } |\mathcal{A}_i| = 2 \text{ and } TA_{i1} \neq TA_{i2} \quad (5)$$

In equation 5,  $\mathcal{A}_i$  is subset of augmentation transformation applied for selected image i.

Every transformation is applied separately to each image to achieve two new augmented images:

$$OD'_{i1} = TA_{i1}(OD_i), \quad OD'_{i2} = TA_{i2}(OD_i) \quad (6)$$

In equation 6,  $OD'_{i1}$  and  $OD'_{i2}$  are the two augmented images after applying  $TA_{i1}$  and  $TA_{i2}$  respectively.

For each original image  $I_i$  two augmented images are collected

$$\mathcal{OD}'_i = \{OD'_{i1}, OD'_{i2}\} \quad (7)$$

The augmented dataset will be:

$$\mathcal{OD}' = \bigcup_{i=1}^{110} \mathcal{OD}'_i, \quad |\mathcal{OD}'| = 110 \times 2 = 220 \quad (8)$$

In equation 8,  $\mathcal{OD}'$  is augmented dataset.

The Final Augmented dataset is:

$$\mathcal{D} = \mathcal{OD} \cup \mathcal{OD}' \Rightarrow |\mathcal{D}| = 110 + 220 = 330 \quad (9)$$

Finally, the 330 OPG radiograph dataset is generated. This method ensures both balance and variability in the dataset, thereby enhancing the model's generalization capacity. The

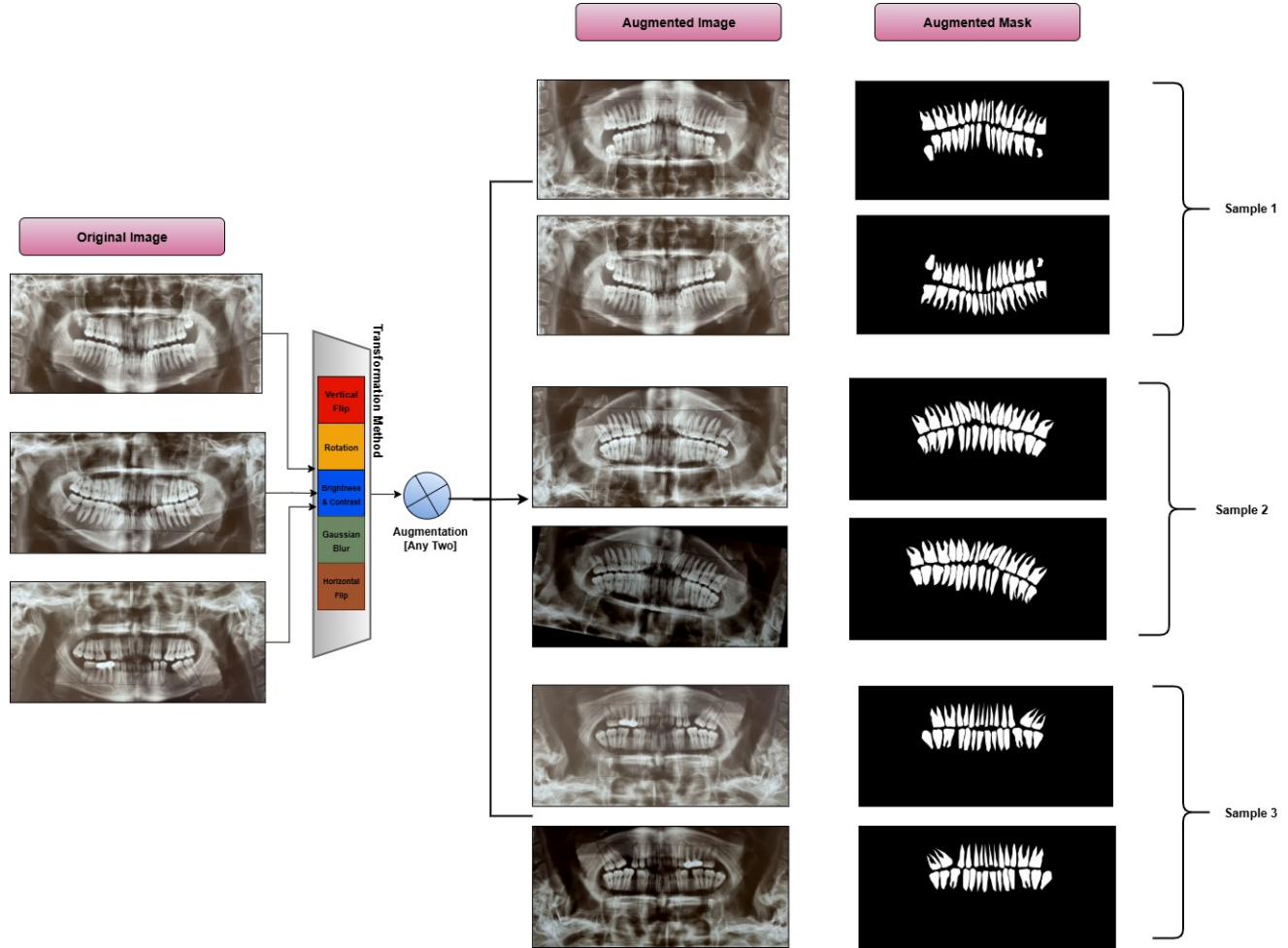


**FIGURE 7.** Augmentation Process with Generated Samples through Conventional Transformations, including Horizontal Flip, Vertical Flip, Rotation ( $\pm 15^\circ$ ), Brightness and Contrast Adjustments, and Gaussian Blur.

augmented samples are shown in Figure 7. The given data augmentation process is a simple mathematical formulation approach given for better understanding purposes. The approach uses very well defined and efficient augmentation techniques used in [55] and [56].

#### 4) Conversion to COCO Format

After completing the augmentation approach, the dataset is converted into a JSON file, further pipelined for COCO format conversion (Common Objects in Context). The COCO format is a widely known annotation structure for instance segmentation. It converts and organizes the image data in a readable format for deep learning models. This format supports bounding boxes, masks, segmentation labels, and more. The detailed algorithm for conversion of mask to COCO format is given in Algorithm 2.

#### E. TOOTH SEGMENTATION USING MASK R-CNN

After analyzing the widely accepted U-Net segmentation algorithm, Mask R-CNN is considered the most relevant approach to execute the proposed algorithm. In this study,

the Mask R-CNN is experimented with and analyzed in two scenarios: with and without augmentation. The architecture of Mask R-CNN is given in Figure 8. The training configuration, parameter and dataset set details for MaskRCNN segmentation with and with augmentation is given in the Table 4. The multiple loss function of MaskRCNN is calculated using the equation 10 which is defined in [59] and [60].

$$\mathcal{L}_{\text{total}} = \mathcal{L}_{\text{RPN-cls}} + \mathcal{L}_{\text{RPN-box}} + \mathcal{L}_{\text{ROI-cls}} + \mathcal{L}_{\text{ROI-box}} + \mathcal{L}_{\text{mask}} \quad (10)$$

The equation 10 consists of classification loss, bounding box regression loss, and mask segmentation loss. Here in the equation 10,  $\mathcal{L}_{\text{RPN-cls}}$  represents the softmax cross-entropy loss used for foreground and background anchor classification,  $\mathcal{L}_{\text{RPN-box}}$  gives Smooth- $\ell_1$  loss for anchor box regression,  $\mathcal{L}_{\text{ROI-cls}}$  shows softmax cross-entropy loss for classification in object-level,  $\mathcal{L}_{\text{ROI-box}}$  gives the bounding box regression loss, and lastly  $\mathcal{L}_{\text{mask}}$  denotes the pixel-level binary cross-entropy loss for mask prediction in Mask R-CNN.

---

**Algorithm 1:** Data Augmentation Procedure for OPG Radiographs

**Input:** Original 110 OPG images and their respective tooth masks  
**Output:** Augmented OPG images and augmented tooth masks

**Function** `Augment-Data()`:

**Define the selected augmentation transforms:**

        // Augmentation methods

- Horizontal flip with probability 0.5;
- Vertical flip with probability 0.5;
- Random rotation within  $\pm 30^\circ$  with probability 0.5;
- Adjusting the contrast with probability 0.2;
- Embedding Gaussian noise with probability 0.2;

**Collect the original 110 OPG radiograph filenames from the input path;**

**foreach** individual image  $I$  **do**

- Add the corresponding mask  $M$ ;
- for**  $i = 0$  **to** 1 **do**

  - Apply transformation on  $(I, M)$ ;
  - Save the augmented image with suffix  $_augi.png$ ;
  - Save the corresponding mask with suffix  $_augis.png$ ;

---

**Algorithm 2:** Conversion of Augmented Tooth Masks to COCO-annotation Format

**Input:** Augmented OPG images  $I$  with respective binary masks  $M$

**Output:** COCO-format JSON annotation file

**Function** `Convert-To-COCO( $I, M$ )`:

**foreach** augmented image  $I$  **do**

- Parse binary mask  $M$  into instances of every tooth using CCA method;

**foreach** tooth **do**

- extract polygon contours;
- encode mask polygons;
- assign info, category ID, bounding box, and area;

    group the instance metadata into the annotations module;

    group the image metadata into the images folder;

After processing all images::  
save category definitions in the categories module;

**prepare a single standard COCO-format JSON file by appending:**

- images
- annotations
- categories

;

**return** COCO-format file

---

1) Overview of Mask R-CNN Architecture

Mask R-CNN is similar to Faster R-CNN with an extra layer for instance segmentation. In this framework, a mask prediction branch is appended, making it more suitable for object detection and high-resolution instance mask generation for every instance. The basic Mask R-CNN model consists of three key modules: the Backbone Network, the Region Proposal Network, and the RoI Align.

*a: Backbone Network– ResNet-50 with Feature Pyramid Network (FPN)*

The backbone of the Mask R-CNN module is built using ResNet-50, which functions to extract hierarchical feature maps. The extracted feature maps are pipelined with a Feature Pyramid Network (FPN) to generate a multi-scale feature representation. The FPN owns the property to perform object detection in varying resolution scales and features. This approach supports OPG radiograph with complex structures.

*b: Region Proposal Network (RPN)*

Region Proposal Network is a Mask R-CNN component that generates a set of anchor boxes by scanning feature maps from FPN using sliding windows. Each anchor box estimates the object score and accuracy of localized objects. Using non-maximum suppression (NMS), findings are filtered and passed to the next step.

**TABLE 4. Training Configuration and Dataset Details for Mask R-CNN**

Category	Parameter	Value
Model Architecture	Backbone	ResNet-50
	Neck	Feature Pyramid Network (FPN)
	Framework	Mask R-CNN
Dataset	Training set	tooth_train (80% of dataset)
	Validation set	tooth_val (20% of dataset)
Input	Mask format Number of classes	Bitmask 1 (tooth)
Training	Batch size (images)	2
	Max iterations	1000
	Learning rate	0.00025
	Learning rate schedule	Constant
	Weight initialization	COCO pretrained
ROI Head	Proposals per image	128
Optimization	Optimizer	SGD
	Momentum	0.9 (default)
	Weight decay	0.0001 (default)
Loss Functions	Classification loss	Cross-entropy
	Bounding box loss	Smooth L1
	Mask loss	Binary cross-entropy
Hardware	GPU	NVIDIA Tesla T4 (16 GB)

*c: RoI Align and Feature Pooling*

RoI align is an operation that extracts the feature maps of a fixed size. It adopts the bilinear interpolation to overcome

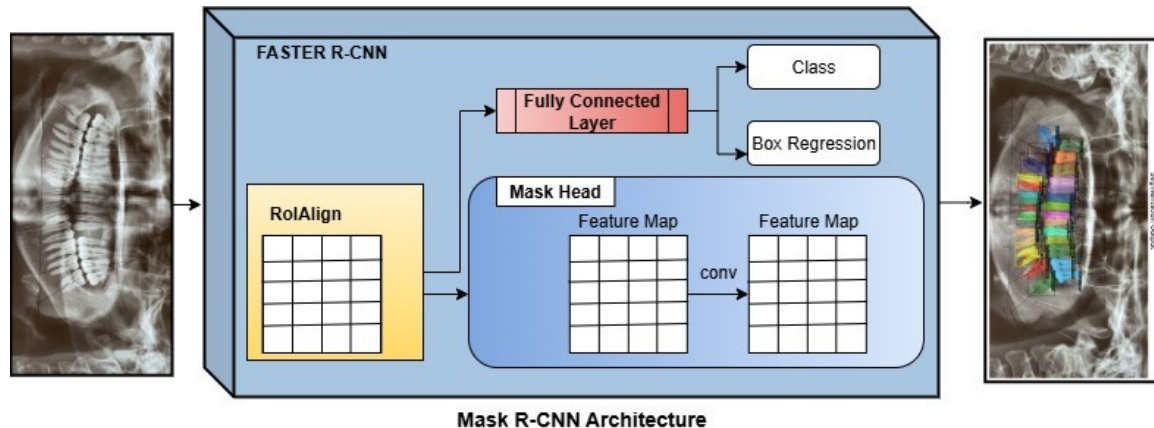


**FIGURE 8.** Structural Overview of Mask R-CNN Architecture Comprising the Backbone Network, Region Proposal Network, and Mask Prediction Branch.

the coordinate quantization limitation. This precise sampling helps in retrieving the minute and delicate contours by preserving the accurate boundaries.

#### *d: Prediction Heads*

The model consists of three heads: classification, bounding box regression, and mask head. During the model training phase, each ROI is passed through the three heads. The Classification head determines the tooth class, and the bounding box regression head determines coordinates. Finally, the mask head analyzes pixel-level precision and object boundary localization.

#### **2) Mask R-CNN Implementation Strategy**

The performance of the Mask R-CNN segmentation model is evaluated using two different conditions: without augmentation and with controlled augmentation. The objective of devising two scenarios is to evaluate generalization, clinical reliability, and statistical improvement. Detectron 2 trains both models in this study.

#### *a: Training Without Data Augmentation*

In the first scenario of training, the model is trained without augmentation, utilizing a manually annotated dataset with OPG images. The "mask\_rcnn\_R\_50\_FPN\_3x" from the Detectron2 model zoo is considered the architecture for the training. The training run on T4 GPU for 1000 iterations with a batch size of 2, and ROI head 128 proposals per image.

#### *b: Training With Controlled Data Augmentation*

In the second scenario, the model was trained with controlled augmentation to enhance generalization. In the augmentation process, the transformations such as Horizontal and vertical flipping, rotations, Contrast and brightness adjustments, and Gaussian blurring are applied. The "mask\_rcnn\_R\_50\_FPN\_3x" from the Detectron2 model zoo is adopted as the architecture for the training. The model undergoes training for 1000 iterations with a batch size of 2,

and 128 ROI proposals per image using the T4 GPU runtime. The outcome analysis of both scenarios is illustrated in the result section.

#### **3) Post-Training Mask Refinement Strategy**

Following the successful completion of OPG segmentation using Mask R-CNN, a post-processing methodology is incorporated to make segmented orthopantomogram radiographs more reliable and suitable for clinical measurements such as angulation, mid-point identification, and others. In the raw output generated by Mask R-CNN, every tooth is masked with an RGB color mask and a bounding box. To remove non-essential visual elements, the bounding box is eliminated, retaining only the pixel color mask. Later, programmatically, the RGB mask is converted to a binary mask to ensure uniformity in the mask for geometrical analysis and enhance compatibility. The post-processed outcomes are illustrated in the results section. This step is highly essential in dental imaging for geometrical analysis to restore clear boundaries and morphological consistency, which is crucial for downstream analysis such as tooth inclination measurement or root structure isolation.

#### **F. TOOTH MIDPOINT DETECTION AND AXIAL LINE CONSTRUCTION IN POST-SEGMENTED OPG IMAGES**

After completing the segmentation process and preprocessing it for clinical requirements, the subsequent objective is to calculate the axial inclination angle of each tooth. The overall workflow of the methodology involves calculating the top and bottom points of each tooth, localizing the central vertical line, and proceeding with further angle calculation.

#### **1) Preprocessing and Binary Mask Generation**

The segmented mask will undergo morphological operations to reduce noise and enhance structural clarity. The morphological opening filter with a kernel size of 5\*5 is used to remove narrow bridges and suppress background noise. The execution of sharpening and erosion will highlight tooth

boundaries and sustain isolated tooth shape using the same filter. The application of the Otsu technique will select the best threshold to reduce intra-class variance. An outcome of a high-contrast binary image in which each component represents a separate connected region. The detailed algorithm is given in Algorithm 3.

**Algorithm 3:** Preprocessing and Standard Binary Mask Generation

**Input:** Grey mask image  $I_{mask} \in \mathbb{G}^{H \times W}$

**Output:** Binary mask image  $I_{binary} \in \{0, 255\}^{H \times W}$

**Function** Binarization–Preprocess ( $I_{mask}$ ) :

Define morphological kernel  $MK$  as a  $5 \times 5$  matrix of ones;

Define sharpening kernel:

$$SK = \begin{bmatrix} -1 & -1 & -1 \\ -1 & 9 & -1 \\ -1 & -1 & -1 \end{bmatrix}$$

For morphological opening to remove small noises:

$$I_{open} = (I_{mask} \ominus MK) \oplus MK$$

Apply sharpening filter:

$$I_{sharp} = I_{open} * SK$$

Perform erosion to enhance boundaries:

$$I_{eroded} = I_{sharp} \ominus MK$$

Compute Otsu threshold:

$$OTSU = \arg \min_T [\sigma_{within}^2(OTSU)]$$

Apply binarization:

$$\text{Standard}I_{binary}(x, y) = \begin{cases} 255 & \text{if } I_{eroded}(x, y) > OTSU \\ 0 & \text{otherwise} \end{cases}$$

**return** Standard $I_{binary}$

## 2) Midpoint Extraction of Segmented Teeth

In the next step, Connected Component Analysis(CCA) is executed to identify and label individual tooth regions. The detected regions are filtered based on the counter area. Retaining only the counter area greater than 2000 pixels, the remaining areas will be discarded. Moreover, the extracted area is free from spurious artifacts. The detailed procedure is given in Algorithm 4.

## 3) Tooth Numbering and Vertical Axis Construction

For the counter area extracted from each region, the minimum area is calculated by enclosing the rectangle using OpenCV. The rectangular box yields four corner coordinate points. The midpoint between the four coordinates is calculated in vertical order to generate a vertical axis line. The midpoints generated

---

**Algorithm 4:** Midpoint Extraction

**Input:** Binary image  $I_{binary}$ , Original RGB image  $I_{RGB}$

**Output:** Top midpoints  $\{M_t^i\}$ , bottom midpoints  $\{M_b^i\}$ , tooth count  $tc$

**Function** Midpoint ( $I_{binary}, I_{RGB}$ ) :

// 1. Execute Connected Component Labeling

$CCL(x, y)$  = label of connected region in  $I_{binary}$

// 2. For each label  $i \neq 0$ :

a. Extract region:  $ER_i \leftarrow (CCL == i)$  ;

b. Calculate contour:  $C_i \leftarrow \partial ER_i$  ;

c. If  $\text{Area}(C_i) < \tau$ , skip (noise threshold  $\tau = 2000$ ) ;

d. Fit minimum-area rectangle:

$rect_i = \text{MinAreaRect}(C_i)$  ;

e. Compute rectangle vertices:

$V = \{v_1, v_2, v_3, v_4\} \in \mathbb{R}^2$  ;

f. Sort  $V$  by Y-coordinate:  $V_{sorted} \leftarrow sort(V)$  such that  $y_1 \leq y_2 \leq y_3 \leq y_4$  ;

g. Define top and bottom points:

$v_t^{(1)} = V_{sorted}[0], v_t^{(2)} = V_{sorted}[1]$  ;

$v_b^{(1)} = V_{sorted}[2], v_b^{(2)} = V_{sorted}[3]$  ;

h. Compute midpoints:  $M_t^i = (\frac{x_1+x_2}{2}, \frac{y_1+y_2}{2})$  ;

$M_b^i = (\frac{x_b1+x_b2}{2}, \frac{y_b1+y_b2}{2})$  ;

i. Store  $M_t^i$  and  $M_b^i$  ;

j. Increment count:  $c \leftarrow c + 1$  ;

**return**  $\{M_t^i\}, \{M_b^i\}, tc$

---

are named as the top midpoint and the bottom midpoint. The vertical axis generated represents the axial orientation and serves as a reference for computing angle deviation. For clarity, each tooth is labelled and annotated with the number. A Command Line Interface (CLI) was developed to classify maxillary and mandibular teeth. The generated midpoints are stored in the array for future reference.

## G. AXIAL INCLINATION CALCULATION

To measure the axial inclination angle of each tooth, two reference lines are mandatory. For maxillary teeth, the top horizontal reference line is obtained by connecting the two orbitale. For mandibular teeth, the bottom reference line is obtained by joining the two mental foramen on both sides. The generation of the reference line and the identification of the reference point is the task of the dentist. The interactive user interface is created for dentists to capture the reference points using a plotly and OpenCV. The OPG radiograph, which needs analysis, is loaded and converted to RGB format using Plotly. A red scatter marker is integrated to add click and read (x,y) coordinates of each reference point using an IPython widget. This method helps to read and identify tooth landmarks, mental foramen, and orbitale for further reference line generation. An interactive visualization tool was created using Plotly and OpenCV to display OPG images and

### Algorithm 5: Numbering and Axis Line Drawing

**Input:** Midpoints  $\{M_t^i, M_b^i\}$ , tooth index ranges for top and bottom teeth

**Output:** Annotated RGB image  $I_{annot}$  with tooth numbers and axis lines

**Function** Draw-Axis( $M_t^i, M_b^i$ ):

1. Initialize annotated image:

$$I_{annot} \leftarrow I_{orig}$$

2. For each tooth index  $i = 1$  to  $c$ :

- a. Draw axis line:

$$cv2.line(I_{annot}, M_t^i, M_b^i, yellow, thickness = 5)$$

- b. Add label at top midpoint:

$$cv2.putText(I_{annot}, str(i), M_t^i - offset, green)$$

- c. If  $i \in [top\_start, top\_end]$ , append  $M_t^i, M_b^i$  to top list

- d. Else if  $i \in [bottom\_start, bottom\_end]$ , append  $M_t^i, M_b^i$  to bottom list

3. Return annotated image:

$$I_{annot}$$

capture user clicks. The image is loaded and converted to RGB format, then shown using Plotly. A red scatter marker is added to allow clicking on specific points. When a point is clicked, its exact (x, y) coordinates are printed in real-time using a callback function and an IPython widget. This helps in manually identifying tooth landmarks and getting a top and bottom horizontal reference line.

Initially, the top midpoint  $M_t(x_t, y_t)$  and bottom midpoint  $M_b(x_b, y_b)$  are calculated for each tooth, which are connected using a vertical axis  $\vec{v}_1 = \overrightarrow{M_1} = (x_b - x_t, y_b - y_t)$ .

The generated vertical axis is further extended to meet the defined occlusal reference plane. Line  $\overline{AB}$  for the maxillary occlusal reference line and Line  $\overline{CD}$  for the mandibular teeth reference line. The maxillary teeth's vertical axis will be linked to the upper occlusal reference line, orbitale. The mandibular teeth's vertical axis is extended to join the lower occlusion reference line and the mental foramen. According to the computational geometry the intersection point between the reference occlusion line and the tooth axis can be calculated using the standard determinant based lines intersection formula as given in [57]. To identify the intersection point with the occlusion reference line, a determinant-based closed-form expression is applied as given below. Assume two line segments defined by points  $(x_1, y_1), (x_2, y_2)$  and  $(x_3, y_3), (x_4, y_4)$ , the intersection point of extended vertical line with occlusion reference line is  $I(x_i, y_i)$  is determined as follows:

$$x = \frac{(x_1y_2 - y_1x_2)(x_3 - x_4) - (x_1 - x_2)(x_3y_4 - y_3x_4)}{\Delta} \quad (11)$$

$$y = \frac{(x_1y_2 - y_1x_2)(y_3 - y_4) - (y_1 - y_2)(x_3y_4 - y_3x_4)}{\Delta} \quad (12)$$

where

$$\Delta = (x_1 - x_2)(y_3 - y_4) - (y_1 - y_2)(x_3 - x_4) \quad (13)$$

This always gives a result where  $\Delta \neq 0$  and  $\Delta$  is intersection determinant.

Subsequently, the angle calculation for axial inclination is achieved using vector algebras, classical vector dot-product formulation for angle estimation between two lines [58]. Consider  $M(x_m, y_m)$  is the midpoint of the tooth axis and  $\vec{v}_1 = \overrightarrow{M_1}$  represent the vector from the tooth midpoint to the intersection point, and  $\vec{v}_2 = \overrightarrow{AB}$  the occlusal line. The endpoints of occlusion reference line is shown as  $A(x_a, y_a)$  and  $B(x_b, y_b)$ . The angle  $\theta$  between them is determined using the dot product:

$$\theta = \cos^{-1} \left( \frac{\vec{v}_1 \cdot \vec{v}_2}{\|\vec{v}_1\| \cdot \|\vec{v}_2\|} \right) \quad (14)$$

Here

- Dot product:

$$\vec{v}_1 \cdot \vec{v}_2 = (x_i - x_m)(x_b - x_a) + (y_i - y_m)(y_b - y_a) \quad (15)$$

- Magnitudes:

$$\|\vec{v}_1\| = \sqrt{(x_i - x_m)^2 + (y_i - y_m)^2}, \quad (16)$$

$$\|\vec{v}_2\| = \sqrt{(x_b - x_a)^2 + (y_b - y_a)^2} \quad (17)$$

- Substituting this value into the angle formula:

$$\theta = \cos^{-1} \left( \frac{(x_i - x_m)(x_b - x_a) + (y_i - y_m)(y_b - y_a)}{\sqrt{(x_i - x_m)^2 + (y_i - y_m)^2} \cdot \sqrt{(x_b - x_a)^2 + (y_b - y_a)^2}} \right) \quad (18)$$

The obtained angle denotes the axial inclination of teeth concerning the occlusal baseline.

## IV. RESULTS AND DISCUSSION

This section presents the results of the novel approach proposed for measuring the angle of axial inclination in three modules. Module 1 outlines the quantitative analysis of the proposed methodology. Module 2 illustrates the result of the angulation, and module 3 demonstrates statistical analysis of the proposed novel model.

### A. QUANTITATIVE ANALYSIS OF SEGMENTATION MODEL

In this module, the quantitative analysis of the proposed segmentation model is conducted for different sets of iterations. To quantitatively analyse the performance, we have chosen four performance metrics, namely, precision, recall, F1 Score, and Intersection over Union.

Precision is the measure of true positives in the union of true positives and false positives. It represents accurately predicted tooth pixels among all the tooth pixels. Generally, it is considered that the higher the precision, the lower the false tooth detection, which can avoid inaccurate calculation of the angle.

Recall (sensitivity) is a measure to quantify the proportion of accurately detected tooth pixels versus all actual tooth pixels. In this study, a high recall value indicates that the segmentation has captured the complete anatomical structure of each tooth without any partial missing teeth in the mask. This will help in finding the correct occlusal reference plane for axial inclination measurement.

The Dice Similarity Coefficient (DSC) is a harmonic mean of precision and recall, balancing both false positives and false negatives. This metric is necessary to assign a single robust score and penalize equally over-segmented teeth and missed tooth pixels.

IoU is a performance metric to quantify the ratio of the overlap area between predicted and ground truth masks to their union. IoU is generally considered a strict metric that provides a low IoU in the case of even a small boundary overall between predicted and ground truth data. In this study, IoU indicates the correct detection contours in the OPG.

In the execution of this study, the segmentation is carried out for both augmented and non-augmented data. The quantitative analysis of both models is performed using precision, recall, F1 Score, and Intersection over Union performance. The quantitative analysis is shown in the Table 5. Figure 13 illustrates the segmented OPG radiographs at 1000 iterations for both the augmented and non-augmented mask R-CNN models. The outcome represents variation inconsistent with the original data distribution, reducing the model accuracy. Moreover, the outcome of augmented segmentation yields inaccurate midpoint detection.

**TABLE 5. Comparative Analysis between Non-Augmented and Augmented Mask R-CNN Segmentation Models for 1000 Iterations**

Metric	Non-Augmented	Augmented
Precision	0.8344	0.7200
Recall	0.9213	0.8000
Dice (F1)	0.8757	0.7579
IoU	0.7788	0.6102

Table 5 illustrates a comparative analysis of the non-augmented and augmented Mask R-CNN segmentation models trained for 1000 iterations. The non-augmented segmentation model performs better with a higher precision of 0.8344 and a recall of 0.9213. A good value of dice score 0.8757 and IoU score 0.7788 is observed. The loss curve of Mask R-CNN segmentation is given in Figure 9.

The training loss curve illustrated in Figure 9 explains a stable converged optimization of the MaskRCNN. The blue curve in the graph represents the total loss, which experiences a rapid decrease in the initial training stage and eventually stabilizes at 1000 iterations with effective convergence and

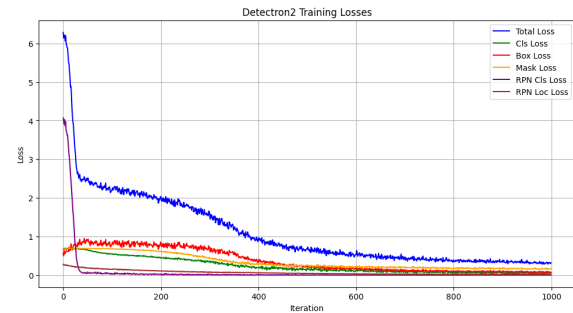


**FIGURE 9. Training Loss Curve for Proposed Mask R-CNN Model.**

learning. The green curve demonstrates the classification loss, indicating clear discrimination between the background and the tooth area. The red curve indicates bounding box region loss with better object localization. The orange curve indicates smooth convergence of mask loss with accurate pixel-level segmentation. Finally, the purple curve shows localization loss and RPN classification. Overall, in the given loss curve for Mask R-CNN, no late-stage loss escalation, overfitting during training, or oscillatory behaviour across the components is seen. Hence, the proposed Mask R-CNN segmentation confirms the robustness of the segmentation. Exhaustive hyperparameter tuning is not included in the current study due to the dataset size and high computational cost. Additionally, a steady performance is observed between the training and validation datasets, with uniform recall, precision, IoU, and Dice. value with the unseen OPG, which demonstrates no overfitting issues in the proposed model.

The augmented model is tested with the same performance metrics for different iteration values as illustrated in the Table 6.

**TABLE 6. Performance Metrics for Augmented Mask R-CNN Segmentation Model**

Iterations	Precision	Recall	Dice (F1)	IoU
200	0.2715	0.9101	0.4182	0.2644
400	0.45	0.89	0.5978	0.4263
600	0.58	0.86	0.6928	0.5300
800	0.66	0.83	0.7353	0.5814
1000	0.72	0.80	0.7579	0.6102

The tabulated results represent the expected evolution of segmentation performance metrics for the augmented Mask R-CNN model across increasing iterations.

The table 6 represents the performance analysis of the Mask R-CNN segmentation model with data augmentation. The model is experimented with 200, 400, 600, 800, and 1000 iterations. The model has a very high recall of 0.91 and a low precision of 0.27, which indicates over-segmentation. Additionally, Dice and IoU outcomes are low due to the quality of the mask overlap. By 400 iterations, the model discards spurious detection and applies convergence where precision increases to 0.45. By 600 iterations, the learning potential is raised in terms of boundaries and contextual relationships.

The precision, Dice, and IoU values are increased. By 800 iterations, an enhancement in regional-level segmentation. Finally, at 1000 iterations, the outcome is 0.72 precision with a recall of 0.80, indicating the model's potential to reduce false positives. The Dice with value 0.7579) and IoU 0.6102, indicates models' suitability for measurement of axial inclination angles. Overall, the designed segmentation approach is reliable.

This demonstrates that the non-augmented segmentation model delivers a better and reliable outcome on the original dataset. The augmented segmentation model falls back in this study with a lower precision of 0.72, which is lower compared to the augmented module. Indeed, the augmentation technique is beneficial. However, in this study, due to the excessive anatomical distortion with respect to datasize, variability in augmentation and number of iterations, the augmented segmentation model falls back. The outcome illustrated by the augmented segmentation model is reliable and can be fine-tuned using optimization, an increase in the number of iterations, and improved augmentation. The visualization of segmentation over the different iteration values is given in Figure 12.

Figure 12 clearly illustrates the segmentation of OPG radiographs using Mask R-CNN with augmentation. The model is executed at 200, 400, 600, and 1000 iterations to analyse the impact of training duration. This execution monitors and evaluates the performance metrics for tooth-wise detection. Lower iteration count, models show the early convergence behaviour. Moreover, the position and contours of the teeth are not marked clearly. It is observed that increasing the iteration will improve the accuracy of tooth identification and contour detection. Training at 200 iterations, the teeth were misidentified; at 400 iterations, a few teeth were not identified; at 600 iterations, the separation was not clear, and at 1000 iterations, all teeth were identified with contours. The comparison facilitates achieving an optimal trade-off between computational cost and segmentation accuracy.

The OPG radiographs collected for this study were acquired from the Carestream 8100SC system at 10 mA, 10.8 s, and 73 kVp in moderate resolution imaging conditions, following high clinical standards at A.B. Shetty Memorial Institute of Dental Sciences. The designed approach captures the relevant and required tooth structures for axial inclination calculation, leading to better outcomes. As a result, the use of special or high-resolution imaging hardware is not mandatory in regular clinical practice. However, minimal brightness adjustment and contrast enhancement are applied to optimize image clarity and segmentation accuracy, ensuring precise delineation of tooth structures.

Although the proposed model presents strong performance, in certain cases, such as low-contrast regions, irregular tooth morphology, and surface wear, the model gives distorted masks and wrong predictions, as shown in Figure 10.

### 1) Generalization Analysis for Proposed Method using Five-Fold Cross-Validation

To analyze the generalization of the proposed Mask R-CNN segmentation in this study, a 5-fold cross-validation strategy is implemented. The dataset of 110 images is divided into 5 folds, where each fold contains 88 training images and 22 testing images. Each fold contains a different combination of training and testing images. The model was trained on the same configuration as shown in Table 4. Since the Google Colab GPU runtime terminates at 1000 iterations for 5-fold cross-validation and limited hardware resources, the study presents generalization based on 500 iterations using 110 images. The figure 11 illustrates loss curves for 5-fold cross-validation at 500 iterations. Fold 1 illustrates the constant reduction in the training with loss. It shows early convergence and even maintenance thereafter. The fold 1 loss curve represents samples with balanced tooth morphology, which facilitates learning discriminative features. Fold 2 shows a small increase in the intermediate loss caused by a uniform convergence. The observation shows that the training set consists of increased invariant attributes. In Fold 3, the convergence trend is very similar to that of Fold 1, with a slightly higher marginal loss representing an imaging artifact and an insufficiently represented tooth shape. Compared to all the 3-folds. The 4th fold shows the lowest loss values, illustrating a favorable training scenario with high annotation consistency. This fold represents improved learning for better accuracy. The Fold 5 behaves very similarly to the Fold 1, 2, and 3, with no instability and abrupt oscillations.

Overall, all five Folds show a clean and uniform downtrend in the training loss. This indicates a reliable convergence of the proposed framework across all five different folds, validating that the consistently chosen learning rate, training configuration, and optimizer are proper. The loss curves in 5-fold indicate no instability in oscillations, non-divergence, nor abrupt spike in loss, which confirms strong generalization across the folds. Finally, there is no final stage loss hike, which confirms the proposed model is not overfitting.

The study also calculated object-level metrics such as AP50, AP75, mAP, along with pixel-level metrics, namely precision, recall, IoU and Dice, as shown in table 7 and table 8.

**TABLE 7. Object-Level Detection Metrics for Proposed Mask R-CNN Across Five Folds**

Fold	AP50	AP75	mAP
Fold 1	41.2840	0.4876	10.4321
Fold 2	27.4760	0.1193	6.1875
Fold 3	19.4638	0.3808	7.6052
Fold 4	50.8826	10.6409	21.0270
Fold 5	43.6068	0.5623	11.2252

The AP50 is considerably high in all five Folds, indicating that detected tooth instances are reliable, and AP75 exhibits little less, indicating difficulty in segmenting overlapped and blurred tooth boundaries. The mAP remains moderate. In pixel-level metrics, the model outputs reliable precision, re-

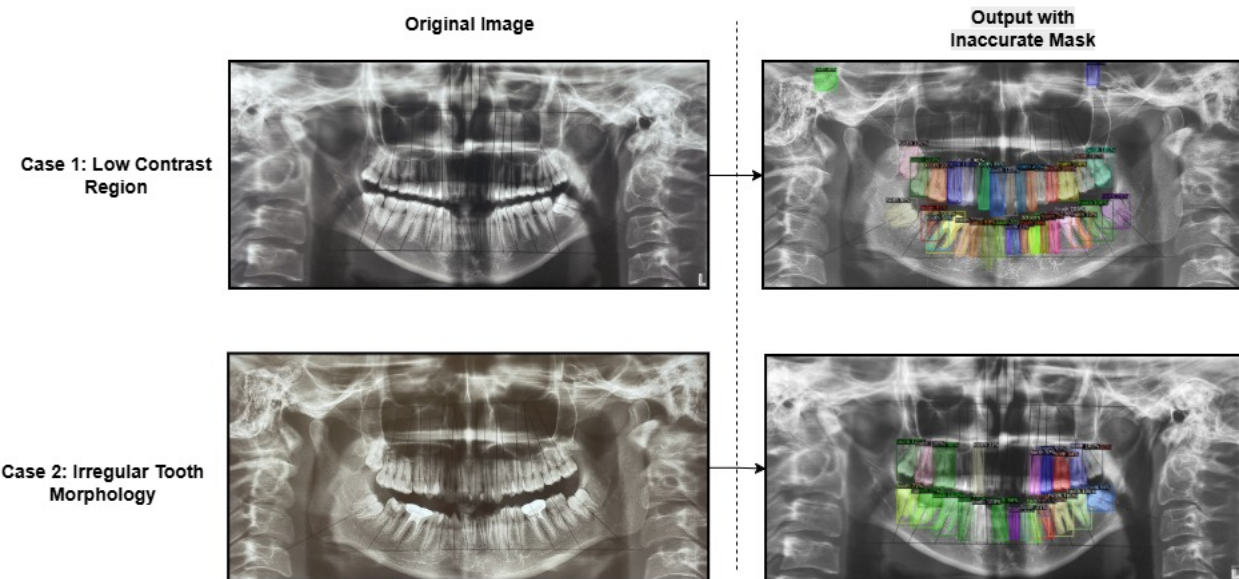


**FIGURE 10.** Error Analysis of Proposed Mask R-CNN Illustrating Original OPG Images and Inaccurate Mask Predicted Corresponding Outputs.

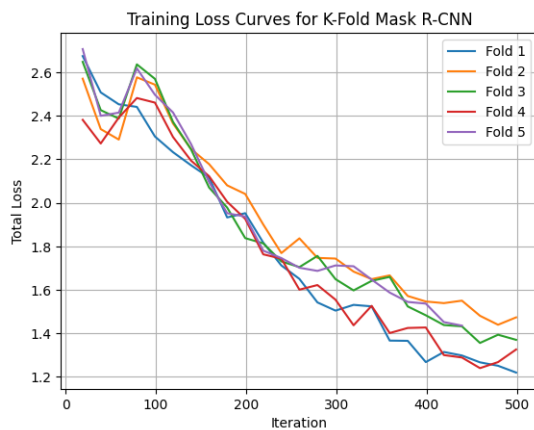


**FIGURE 11.** Training Loss Curve for Proposed Mask R-CNN model with 5-Fold Cross-Validation.

**TABLE 8.** Pixel-Level Segmentation Metrics for Proposed Mask R-CNN Across Five Folds

Fold	Precision	Recall	Dice (F1)	IoU
Fold 1	0.7982	0.6024	0.6731	0.5189
Fold 2	0.7426	0.4873	0.5694	0.4217
Fold 3	0.7611	0.5038	0.6129	0.4482
Fold 4	0.8345	0.6481	0.7216	0.5619
Fold 5	0.8096	0.6185	0.6913	0.5328

call, Dice, and IoU, showing consistent tooth masks even on different training and testing dataset splits. Finally, the proposed method demonstrates considerable performance for pixel and object-level metrics at 500 iterations, which is expected to improve at 1000 iterations, as shown in the table 5 at non-fold cross-validation technique.

## B. COMPARATIVE EVALUATION OF SEGMENTATION MODELS WITH EXISTING METHODS

This section presents an in-depth qualitative and quantitative evaluation of the proposed Mask R-CNN instance segmentation model in comparison to the existing literature and the proposed semantic-based U-Net segmentation model. Additionally, the section explains the clinical relevance and computational efficiency of choosing instance segmentation over semantic segmentation.

**TABLE 9.** Segmentation Performance Comparison of Existing Methods and the Proposed Model

Method	Precision	Recall	Dice (F1)	IoU	Type
Vanilla U-Net [18] epochs:100	—	—	89.53	88.22	Semantic
Attention U-Net [18] epochs:100	—	—	89.78	88.39	Semantic
Proposed U-Net epochs:130	0.9019	0.9136	90.77	83.10	Semantic
Proposed Mask R-CNN epochs: ( $\approx$ 11–18)	0.8344	0.9213	87.57	77.88	Instance

Table 9 presents the segmentation performance of existing U-Net variants and the proposed Mask R-CNN model, in terms of accuracy, precision, recall, Dice, and IoU. More emphasis is given to precision, recall, dice, and IoU to strengthen the dental OPG medical segmentation.

The proposed U-Net and existing literature vanilla and

Attention U-Net have high accuracy and dice score, but face issues in blurred OPG and merged teeth cases. The proposed U-Net model requires more than 24 hours to run 130 epochs with a batch size of 4, approximately 3640 iterations, and failed to preserve inter-tooth boundaries. In contrast, the proposed Mask R-CNN takes approximately 3 hours to run 1000 iterations. The dice and IoU of the proposed MaskRCNN are lower, which is expected in instance segmentation, but gives accurate tooth shapes, which is most needed for mesiodistal angulation. Therefore, in our study with a major aim to calculate mesiodistal angulation, Mask R-CNN was selected due to its computational efficiency, clinical stability for tooth-wise angle analysis, and superior instance-level segmentation.

### C. ANGULATION MODULE OUTCOME

This section presents the outcomes from analyzing tooth angulation using the OPG radiographs. The Mask R-CNN segmentation output displays bounding boxes representing each tooth on the segmented OPG image. In the Figure 13, the detected bounding boxes are not uniformly aligned with each tooth. Moreover, the rectangle bounding each tooth includes the background pixel, as well as other pixels of adjacent teeth in an overlapping case. In such cases, drawing a centerline from the midpoint to obtain a referential vertical axis will lead to a large deviation. It is concluded that identifying the midpoint based on bounding boxes does not yield accurate midpoints. Consequently, bounding boxes are omitted from the practical Mask R-CNN output to favour accurate midpoint detection as shown in Figure 14. A comparative analysis is carried out between the proposed segmentation and existing segmentation models for the OPG radiograph in [28] and [37]. The proposed segmentation model outperforms the existing models, attaining a precision of 0.83 and a recall of 0.92. The existing algorithm in [28] shows a precision of 0.82 and a recall of 0.77. In the existing algorithm in [37], using mask R-CNN precision is 0.80, and the recall is 0.55. It can be concluded that the proposed segmentation model is better than the existing segmentation model for tooth segmentation.

Prior to angulation, the coloured masked output is converted to a binary mask output to generate a suitable mask for geometric and perfect contour detection. By converting each RGB tooth mask to 1 and the background mask to 0, it provides a noise-free mask for further calculations. For each tooth in the segmented mask, the reference vertical axis is calculated in reference to the midpoint generation. The upper extremity midpoint and lower extremity midpoint of each tooth are calculated using the arithmetic mean of the corresponding extreme horizontal point in the horizontal axis line. The figure 15 illustrates the output of the midpoint detection of each tooth with reference vertical axis in yellow color. In some cases, the vertical axis of the deviated tooth is also clearly observed, especially in the cases of unerupted teeth.

After vertical axis generation, the horizontal reference line is drawn on the basis of the mental foramen and orbitale landmarks, as explained in the methodology section. The

generated vertical reference line is extended to the respective horizontal line to detect midpoints. For this approach, initially intersection points are calculated and marked in the figure 16. Later, the intersection points are connected using a vertical line as shown in the Figure 17.

Finally, using the figure 17, the axial inclination angle of each tooth is calculated. The calculated angle value is displayed in console output, and an option is given to move the cursor to the reference point and obtain the angle. Minor discrepancies and error rates are noted in marginal misalignments and overlap cases, which will be examined in detail in the statistical section.

### D. STATISTICAL ANALYSIS

The study aimed at developing a digital method using the principles of artificial intelligence for measuring axial inclination of teeth in OPG and to assess its reliability. The study included panoramic radiographs of 110 individuals in the age group of 18-30 years who had visited the Department of Orthodontics and Dentofacial Orthopaedics at A. B. Shetty Memorial Institute of Dental Sciences, Mangalore.

The data was entered in Microsoft Excel and analyzed using SPSS version 23. The data were subjected to the Shapiro-Wilk test for testing the normality. The homogeneity of variance assumption was tested by using the Levene statistic for homogeneity of variance. The variables were following a normal distribution. Hence, a parametric evaluation was adopted. The data was analyzed for descriptive and inferential statistics. Descriptive statistics are expressed as mean and standard deviation. The difference between AI and manual measurements was analyzed using an unpaired t-test.  $p < 0.05$  was considered significant. To compare the AI-generated and manual measurements, the mean values and standard deviations (SD) were calculated for each group. The t-statistic was calculated as the difference between group means divided by the standard error of the difference [61]:

$$t = \frac{\bar{X}_{AI} - \bar{X}_{Manual}}{\sqrt{\frac{s_{AI}^2}{n_{AI}} + \frac{s_{Manual}^2}{n_{Manual}}}} \quad (19)$$

Where  $X$  represents the group mean,  $s^2$  the variance, and  $n$  is the sample size of each group. Degrees of freedom were calculated using the Welch-Satterthwaite approximation to account for potential unequal variances. A  $p$ -value  $< 0.05$  was considered statistically significant. The statistical analysis is carried out in quadrant wise and recorded in four separate tables. Table 10 represents Manual and AI generated values of Axial inclination of teeth in 1st quadrant. Table 11 represents Manual and AI generated values of Axial inclination of teeth in 2nd quadrant. Table 12 represents Manual and AI generated values of Axial inclination of teeth in 3rd quadrant. Table 13 represents Manual and AI generated values of Axial inclination of teeth in 4th quadrant.

In the current article, after executing statistical analysis, it is observed there is no statistically significant difference in the axial inclination of teeth as measured manually and by

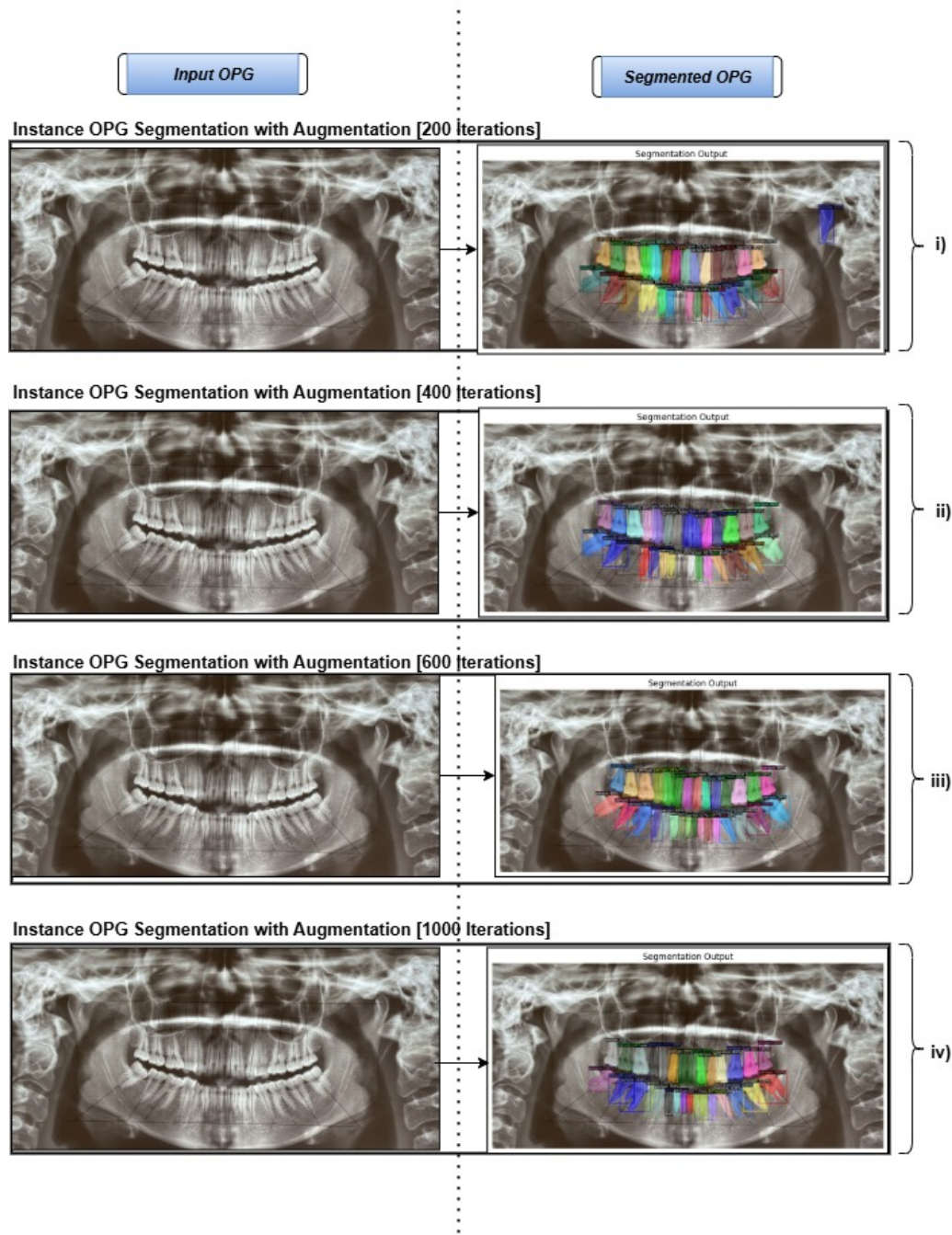


**FIGURE 12.** Mask R-CNN Segmentation With Augmentation Across Different Training Iterations (200, 400, 600, 1000).

using AI, indicating that both the methods have comparable accuracy except with teeth no 21,23,25,26,43. The p-value obtained was less than 0.05. According to clinical experts and dentists, the p-value is less than the threshold considered significant and suitable for clinical trials. Hence using AI to measure the axial inclination angle of tooth in clinical practice is reliable. The graphical wise analysis for each quadrant is shown in Figure 19, 20, 21, and 22. The Figure 18 represents console output which determines the angulation value for an individual tooth based on reference axis calculations.

The graphs 19, 20, 21, and 22 illustrate the comparative analysis of the angulation value of the teeth obtained by the manual and the proposed AI method. The mean of the all 110 OPG radiographs are used for the analysis and its clearly observed only some minor discrepancies are recorded which can be neglected in clinical use. Furthermore, a few samples of the angle of the teeth obtained from the AI driven and manual calculation is shown for reference purposes in Table 14.

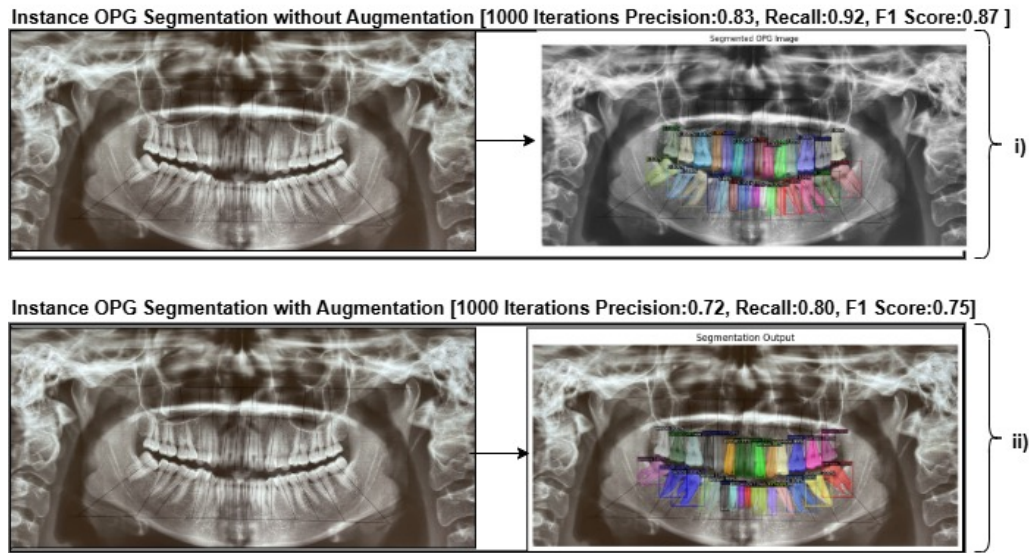


**FIGURE 13.** Comparative Mask R-CNN Model Segmentation Performance With and Without Augmentation at 1000 Iterations.



**FIGURE 14.** Visualization of the Mask R-CNN Model Segmentation Result outlining Predicted Masks without Bounding Box Overlays.

## V. CONCLUSION

This paper presents a novel framework to automate mesiodistal angle calculation from OPG radiographs using deep learning and custom computer vision algorithms. The designed methodology incorporates instance segmentation to extract the contour of teeth and identify the midpoint of each tooth. The experiment is conducted for both augmented and non-augmented techniques, and the augmented technique proved better in highlighting the significance of the model, training stability, and data quality. The generalization of the proposed approach is illustrated using 5-fold cross-validation. The identified midpoints and reference vertical and occlusal axis contribute significantly to calculating mesiodistal inclination. The computed angle is statistically validated against manually measured values by clinical experts, and dentists

confirm that the measurement of the axial inclination based on deep learning shows potential for integration into clinical diagnostics.

The designed approach delivers faster mesiodistal axial inclination calculation with less processing time and reduced human intervention. In the current approach, discrepancy in mesiodistal angulation is noticed in teeth numbers 21, 22, 23, 25, 26, and 27. The malocclusion case study is excluded from the current study. In future work, overcoming angle discrepancy and including malocclusion cases using multi-modal datasets is outlined. Additionally, future work focuses on increasing the size of the data set to achieve better generalization for various patient conditions. Moreover, augmented segmentation demands improvement by increasing the number of iterations and the runtime environment.

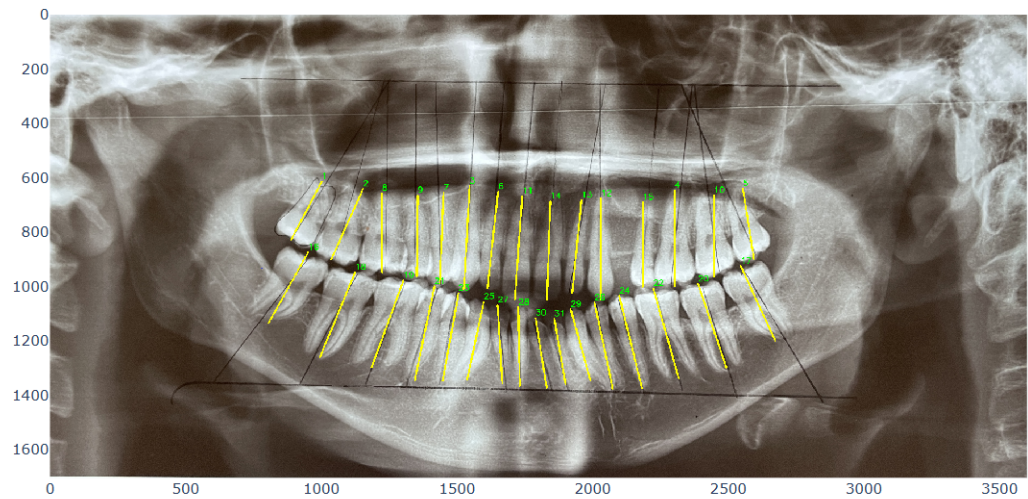


**FIGURE 15.** Detection of the Midpoint and Construction of a Vertical Reference Axis for Anatomical Orientation in OPG Radiographs.

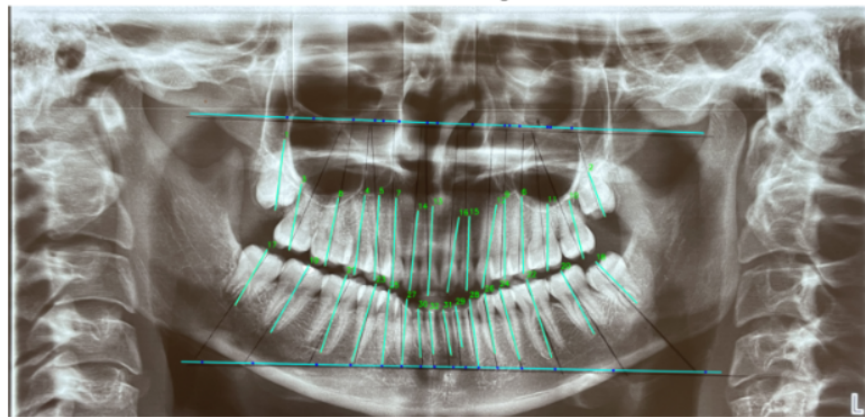


**FIGURE 16.** Horizontal Reference Line Construction and Intersection Points Detection With Its Vertical Reference Axis for Anatomical Orientation in OPG Radiographs.

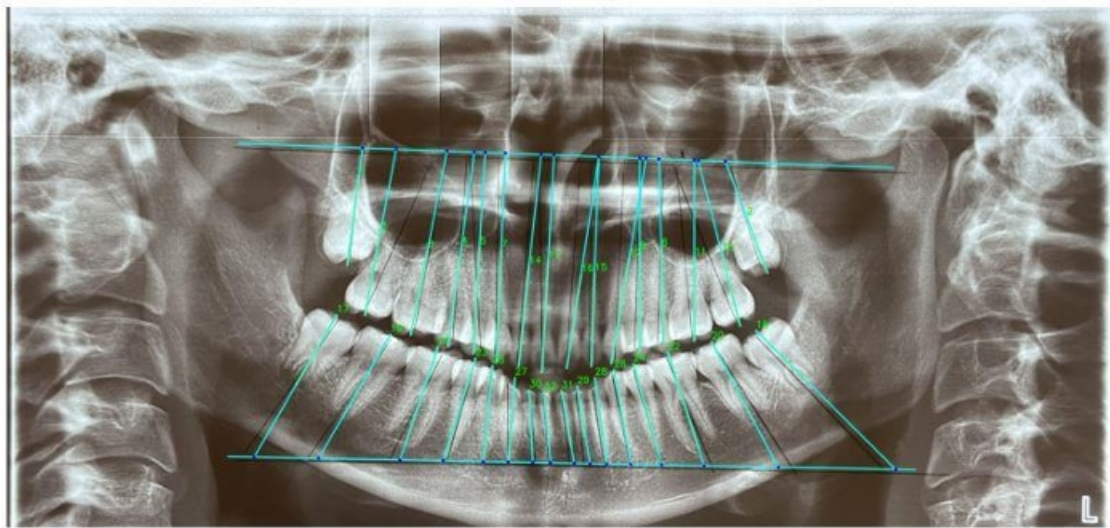


**FIGURE 17.** Axial Inclination Angle Computation Based on the Intersection Point of the Vertical Reference Axis and the Horizontal Reference Line in OPG Radiographs.

Tooth 1: Angle 1 = 62.71 degrees, Angle 2 = 117.16 degrees  
Tooth 2: Angle 1 = 66.31 degrees, Angle 2 = 113.67 degrees  
Tooth 3: Angle 1 = 87.37 degrees, Angle 2 = 92.56 degrees  
Tooth 4: Angle 1 = 90.65 degrees, Angle 2 = 89.34 degrees  
Tooth 5: Angle 1 = 99.61 degrees, Angle 2 = 80.38 degrees  
Tooth 6: Angle 1 = 84.29 degrees, Angle 2 = 95.61 degrees  
Tooth 7: Angle 1 = 88.32 degrees, Angle 2 = 91.61 degrees  
Tooth 8: Angle 1 = 90.58 degrees, Angle 2 = 89.41 degrees  
Tooth 9: Angle 1 = 89.80 degrees, Angle 2 = 90.14 degrees  
Tooth 10: Angle 1 = 91.05 degrees, Angle 2 = 88.86 degrees  
Tooth 11: Angle 1 = 86.56 degrees, Angle 2 = 93.38 degrees  
Tooth 12: Angle 1 = 90.71 degrees, Angle 2 = 89.26 degrees  
Tooth 13: Angle 1 = 84.93 degrees, Angle 2 = 95.07 degrees  
Tooth 14: Angle 1 = 88.67 degrees, Angle 2 = 91.27 degrees  
Tooth 15: Angle 1 = 90.55 degrees, Angle 2 = 89.34 degrees  
Tooth 16: Angle 1 = 118.29 degrees, Angle 2 = 61.84 degrees  
Tooth 17: Angle 1 = 64.03 degrees, Angle 2 = 116.28 degrees  
Tooth 18: Angle 1 = 111.66 degrees, Angle 2 = 68.48 degrees  
Tooth 19: Angle 1 = 109.04 degrees, Angle 2 = 70.97 degrees  
Tooth 20: Angle 1 = 70.19 degrees, Angle 2 = 109.97 degrees  
Tooth 21: Angle 1 = 100.77 degrees, Angle 2 = 79.30 degrees  
Tooth 22: Angle 1 = 73.09 degrees, Angle 2 = 107.04 degrees  
Tooth 23: Angle 1 = 99.21 degrees, Angle 2 = 80.87 degrees  
Tooth 24: Angle 1 = 74.85 degrees, Angle 2 = 105.26 degrees  
Tooth 25: Angle 1 = 101.01 degrees, Angle 2 = 79.06 degrees  
Tooth 26: Angle 1 = 76.83 degrees, Angle 2 = 103.25 degrees  
Tooth 27: Angle 1 = 85.53 degrees, Angle 2 = 94.51 degrees  
Tooth 28: Angle 1 = 87.92 degrees, Angle 2 = 92.15 degrees  
Tooth 29: Angle 1 = 73.05 degrees, Angle 2 = 106.98 degrees  
Tooth 30: Angle 1 = 79.76 degrees, Angle 2 = 100.32 degrees  
Tooth 31: Angle 1 = 78.91 degrees, Angle 2 = 101.12 degrees

**FIGURE 18.** Console Output: Determining the Angulation Value for an Individual Tooth Based on Reference Axis Calculations.

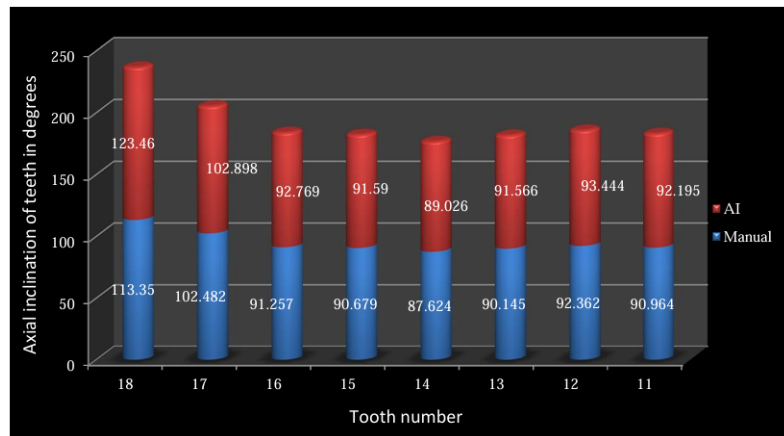


**FIGURE 19.** Comparative Study of Manual and AI-Derived Measurements in First Quadrant Teeth for Angulation Assessment.

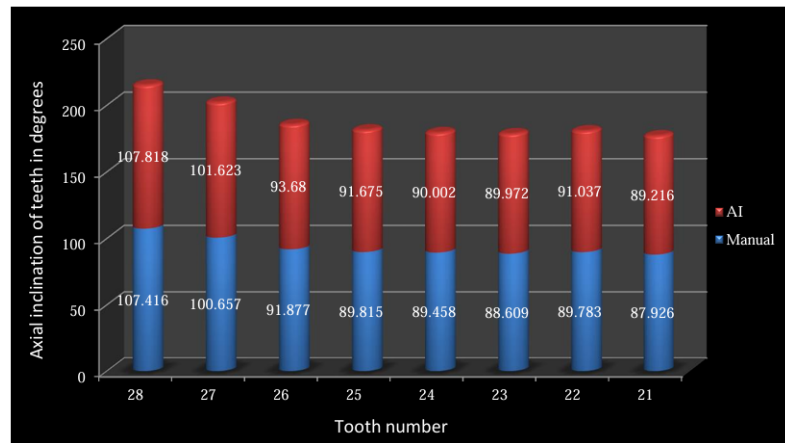


**FIGURE 20.** Comparative Study of Manual and AI-Derived Measurements in Second Quadrant Teeth for Angulation Assessment.

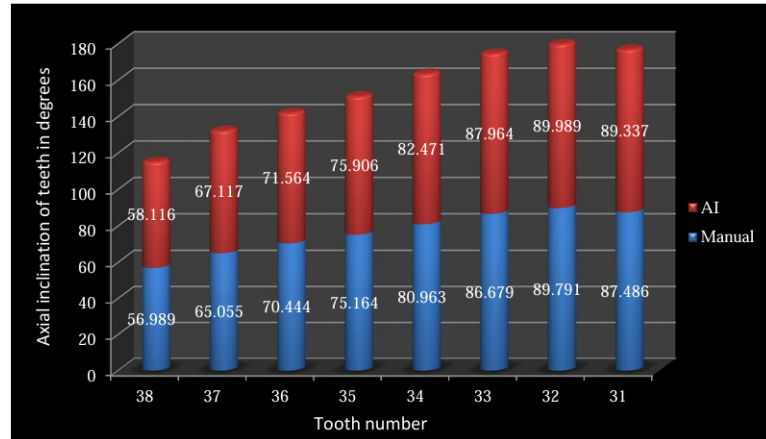


**FIGURE 21.** Comparative Study of Manual and AI-Derived Measurements in Third Quadrant Teeth for Angulation Assessment.

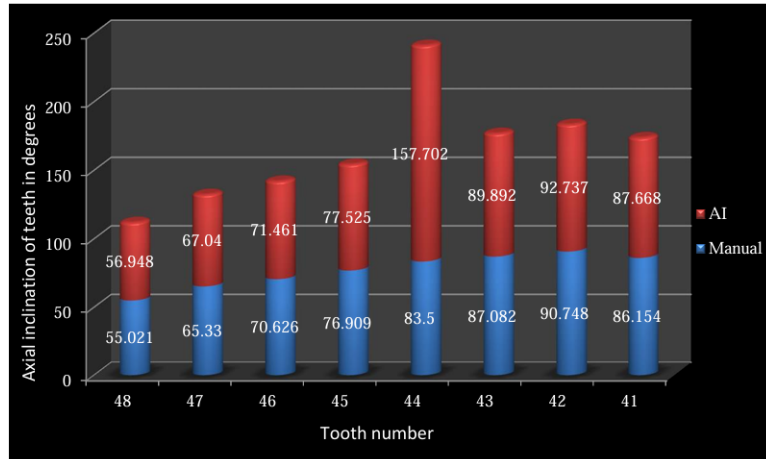


**FIGURE 22.** Comparative Study of Manual and AI-Derived Measurements in Fourth Quadrant Teeth for Angulation Assessment.

**TABLE 10.** Manual and AI generated values of Axial inclination of teeth in 1st quadrant

Tooth No.	Methods	N	Mean	Std. Deviation	Std. Error Mean	95% Confidence Interval of the Difference		Mean Difference	Std. Error Difference	t	p value
						Lower	Upper				
18	Manual	88	113.35	12.42	1.32	-30.205	9.981	-10.112	10.181	-0.993	0.322
	AI	88	123.46	94.69	10.09						
17	Manual	110	102.482	9.511	0.907	-3.566	2.734	-0.416	1.598	-0.260	0.795
	AI	110	102.898	13.803	1.316						
16	Manual	110	91.257	6.832	0.654	-3.364	0.339	-1.512	0.939	-1.610	0.109
	AI	110	92.769	7.033	0.674						
15	Manual	110	90.679	5.791	0.555	-2.463	0.642	-0.911	0.788	-1.157	0.249
	AI	110	91.590	5.838	0.559						
14	Manual	110	87.624	6.067	0.587	-3.070	0.266	-1.402	0.846	-1.657	0.099
	AI	110	89.026	6.308	0.610						
13	Manual	110	90.145	8.115	0.774	-3.685	0.845	-1.420	1.149	-1.236	0.218
	AI	110	91.566	8.912	0.850						
12	Manual	110	92.362	5.995	0.585	-2.795	0.631	-1.082	0.869	-1.245	0.214
	AI	110	93.444	6.584	0.643						
11	Manual	110	90.964	5.050	0.482	-2.749	0.286	-1.231	0.770	-1.599	0.111
	AI	110	92.195	6.303	0.601						

**TABLE 11.** Manual and AI generated values of Axial inclination of teeth in 2nd quadrant

Tooth No.	Method	N	Mean	Std. Deviation	Std. Error Mean	95% Confidence Interval of the Difference		Mean Difference	Std. Error Difference	t	p value
						Lower	Upper				
28	Manual	89	107.416	17.910	1.898	-6.111	5.306	-0.402	2.893	-.139	0.890
	AI	89	107.818	20.589	2.182						
27	Manual	110	100.657	11.435	1.090	-4.113	2.179	-0.967	1.596	-0.606	0.545
	AI	110	101.623	12.228	1.166						
26	Manual	110	91.877	6.265	0.609	-3.534	-0.071	-1.802	0.878	-2.052	0.041*
	AI	110	93.680	6.520	0.633						
25	Manual	110	89.815	4.681	0.450	-3.204	-0.516	-1.860	0.682	-2.728	0.007*
	AI	110	91.675	5.320	0.512						
24	Manual	110	89.458	6.350	0.614	-2.319	1.232	-0.544	0.901	-0.604	0.547
	AI	110	90.002	6.817	0.659						
23	Manual	110	88.609	4.495	0.429	-2.716	-0.011	-1.363	0.686	-1.987	0.048*
	AI	110	89.972	5.620	0.536						
22	Manual	110	89.783	4.856	0.472	-2.594	0.087	-1.253	0.680	-1.843	0.067
	AI	110	91.037	5.046	0.490						
21	Manual	110	87.926	4.011	0.386	-2.509	-0.071	-1.290	0.619	-2.086	0.038*
	AI	110	89.216	5.023	0.483						

## CONFLICT OF INTEREST

The authors declare no conflict of interest.

**TABLE 12.** Manual and AI generated values of Axial inclination of teeth in 3rd quadrant

Tooth No.	Method	N	Mean	Std. Deviation	Std. Error Mean	95% Confidence Interval of the Difference		Mean Difference	Std. Error Difference	t	p value
						Lower	Upper				
28	Manual	89	107.416	17.910	1.898	-6.111	5.306	-0.402	2.893	-.139	0.890
	AI	89	107.818	20.589	2.182						
27	Manual	110	100.657	11.435	1.090	-4.113	2.179	-0.967	1.596	-0.606	0.545
	AI	110	101.623	12.228	1.166						
26	Manual	110	91.877	6.265	0.609	-3.534	-0.071	-1.802	0.878	-2.052	0.041*
	AI	110	93.680	6.520	0.633						
25	Manual	110	89.815	4.681	0.450	-3.204	-0.516	-1.860	0.682	-2.728	0.007*
	AI	110	91.675	5.320	0.512						
24	Manual	110	89.458	6.350	0.614	-2.319	1.232	-0.544	0.901	-0.604	0.547
	AI	110	90.002	6.817	0.659						
23	Manual	110	88.609	4.495	0.429	-2.716	-0.011	-1.363	0.686	-1.987	0.048*
	AI	110	89.972	5.620	0.536						
22	Manual	110	89.783	4.856	0.472	-2.594	0.087	-1.253	0.680	-1.843	0.067
	AI	110	91.037	5.046	0.490						
21	Manual	110	87.926	4.011	0.386	-2.509	-0.071	-1.290	0.619	-2.086	0.038*
	AI	110	89.216	5.023	0.483						

**TABLE 13.** Manual and AI generated values of Axial inclination of teeth in 4th quadrant

Tooth No.	Method	N	Mean	Std. Deviation	Std. Error Mean	95% Confidence Interval of the Difference		Mean Difference	Std. Error Difference	t	p value
						Lower	Upper				
48	Manual	96	55.021	20.808	2.124	-8.043	4.189	-1.927	3.100	-0.622	0.535
	AI	96	56.948	22.132	2.259						
47	Manual	110	65.330	12.001	1.166	-5.114	1.694	-1.710	1.727	-0.990	0.323
	AI	110	67.040	13.115	1.274						
46	Manual	110	70.626	8.839	0.854	-3.340	1.671	-.834	1.271	-0.656	0.512
	AI	110	71.461	9.733	0.941						
45	Manual	110	76.909	10.601	1.011	-3.407	2.174	-0.616	1.416	-0.435	0.664
	AI	110	77.525	10.400	0.992						
44	Manual	110	83.500	7.573	0.729	-218.960	70.556	-74.202	73.440	-1.010	0.313
	AI	110	157.702	763.169	73.436						
43	Manual	110	87.082	10.880	1.037	-5.381	-0.239	-2.810	1.304	-2.154	0.032*
	AI	110	89.892	8.292	0.791						
42	Manual	110	90.748	11.538	1.115	-5.168	1.190	-1.989	1.612	-1.234	0.219
	AI	110	92.737	12.045	1.164						
41	Manual	110	86.154	18.633	1.818	-6.586	3.556	-1.515	2.572	-0.589	0.556
	AI	110	87.668	18.640	1.819						

**TABLE 14. Reference Illustration of Angulation Values Obtained Through AI and Manual Measurements for a Few Teeth.**

MANUAL		AI		MANUAL		AI		MANUAL		AI		MANUAL		AI	
17	17	16	16	15	15	14	14	13	13	14	14	13	13	14	14
106	102.78	97	95.56	98	96.45	94	93.22	100	97.35	90	93.12	93	95.48	96	87.92
100	97.45	88	87.66	100	90.11	93	97.23	97	95.23	87	92.35	93	95.48	90	101.23
110	112.32	97	90.14	90	89.75	95	97.25	87	88.56	92	89.16	101	105.15	94	94.47
101	102.48	90	84.28	105	110.78	89	81.68	90	92.32	80	79.58	95	97.86	98	90.5
113	110.32	90	92.5	111	115.45	93	95.75	105	101.32	75	89.77	85	89.15	100	98.12
120	118.22	82	94.2	97	100.78	86	88.23	86	85.65	85	88.09	85	89.45	88	90.26
100	103.55	87	94.3	98	100.98	92	92.33	87	86.64	85	92.39	95	97.45	95	94.77
108	107.12	98	98.33	95	99.45	93	92.46	100	97.55	86	97.15	88	88.45	92	90.5
101	105.32	97	106.4	95	92.45	90	92.21	100	101.23	80	82.56	91	99.15	90	92.6
102	100.23	82	79.65	90	91.78	80	78.35	90	89.38	85	87.15	91	95.15	80	83.44
100	97.45	92	92.47	87	90.48	92	91.35	88	85.45	87	90.25	88	89.15	85	86.13
98	95.32	89	77.65	96	94.78	89	90.91	95	94.25	85	87.82	95	95.12	92	93.6
110	108.11	97	100.44	97	95.66	83	85.3	98	97.23	93	95.32	91	95.15	91	88.23
105	102.45	93	90.8	100	98.75	94	99.91	95	94.65	83	83.14	91	96.15	92	94.74
117	116.22	85	88.39	95	94.77	94	94.34	90	93.24	91	92.35	90	78.15	95	93.5
105	102.75	78	82.47	92	90.63	97	95.8	90	89.55	86	84.72	80	79.15	85	83.12
100	99.54	82	88.21	94	90.32	85	83.55	83	80.54	76	78.21	86	85.15	86	85.74
100	106.21	80	83.61	88	90.45	73	81.83	90	87.35	90	87.09	96	94.15	75	75.12
91	92.45	83	84.01	97	95.45	91	88.28	90	87.35	85	87.05	96	94.15	90	90.12
116	112.39	77	82.08	98	100.78	99	97.43	97	100.58	85	82.11	87	85.75	82	79.54
107	105.11	94	99.23	97	98.95	80	88.65	92	92.32	90	88.78	81	83.15	85	83.12
120	118.45	78	76.89	81	90.12	80	83.25	81	80.22	89	90.07	93	90.15	88	87.23
92	90.54	91	90.07	93	90.78	87	91.38	83	85.65	87	88.35	79	83.15	93	94.29
106	109.77	88	88.5	98	105.32	95	93.65	93	90.25	91	93.65	85	81.15	91	96.18
120	123.32	97	95.45	80	85.45	79	84.5	91	90.23	83	88.54	83	80.12	87	88.72
73	74.44	80	79.9	88	93.21	87	93.11	90	91.45	85	87.21	81	80.12	95	94.19
102	105.78	75	79.95	87	92.94	93	89.5	85	92.12	93	92.93	92	90.12	87	85.96
120	118.45	78	76.89	81	90.12	80	83.25	81	80.22	89	90.07	91	93.45	95	94.41
92	90.54	91	90.07	93	90.78	87	91.38	83	85.65	87	88.35	79	83.15	89	88.69
106	109.77	88	88.5	98	95.37	92	95.87	93	92.63	95	99.39	75	77.32	87	90.14
110	113.74	92	89.12	87	91.74	91	87.74	83	80.22	87	88.98	89	93.44	97	94.53
91	95.95	84	84.43	92	94.56	90	92.46	77	76.33	87	92.39	91	93.77	89	87.2
109	110.21	94	98.93	88	90.45	95	97.1	95	94.32	91	92.06	84	88.47	88	88.45
95	97.45	99	92.58	101	104.65	100	105.65	95	93.45	96	94.35	90	78.98	94	91.88
113	115.78	82	83.45	99	104	95	97.47	95	94.35	90	92.2	76	78.98	89	88.69
116	117.45	98	95.37	92	95.87	83	83.65	94	93.15	76	77.33	93	95.64	89	93.07
110	113.74	92	89.12	87	91.74	94	97.56	77	92.32	94	92.88	75	80.22	90	88.48
106	102.78	92	95.88	90	93.32	88	97.74	94	93.11	101	99.12	87	88.56	73	71.23
100	98.78	94	97.23	101	99.32	88	87.98	97	95.78	78	80.01	92	90.56	83	83.14
94	87.68	86	87.98	88	90.12	90	95.65	93	93.65	72	79.45	80	78.65	90	82.45
95	98.94	89	90.56	94	90.22	95	95.33	85	93.45	91	93.38	90	92.84	94	94.5
93	90.54	93	95.45	100	103.32	83	83.65	94	93.15	76	77.33	93	95.64	97	93.07
108	105.89	87	97.78	94	97.56	77	92.32	94	92.88	75	72.56	103	100.23	103	100.45
115	113.74	92	95.88	90	93.32	88	97.74	94	93.11	87	99.12	87	88.56	94	95.45
106	102.78	84	87.96	82	85.32	86	85.32	86	87.56	85	87.56	89	87.48	93	97.545
100	98.78	101	100.21	87	90.12	91	89.32	92	95.33	88	87.51	86	85.45	98	100.56
92	90.45	91	95.23	98	100.32	85	83.65	93	95.78	94	90.23	85	87.59	89	94.55
110	114.25	95	94.12	97	100.45	101	100.21	95	95.55	90	95.64	90	93.34	89	87.45
111	114.23	93	90.54	97	100.32	90	95.62	92	97.45	89	92.77	88	85.12	95	88.45
98	100.23	98	96.64	94	90.23	97	95.45	99	105.44	93	90.23	89	90.23	97	100.45
115	117.52	91	95.12	78	85.32	93	90.12	92	95.66	94	93.15	87	90.35	30	27.45
100	102.78	87	90.78	91	95.23	100	97.65	80	83.45	80	83.45	91	90.23	93	97.545
95	98.22	88	90.11	88	90.12	95	93.23	87	90.44	91	94.25	83	82.45	90	94.55
110	114.25	86	89.32	98	100.45	95	90.12	93	97.85	84	86.15	85	82.45	94	99.45
111	114.23	95	94.12	86	89.32	90	95.62	85	82.44	94	92.44	86	88.8	100	110.45
98	100.23	98	96.64	94	90.23	97	95.45	99	105.44	93	90.23	89	90.23	88	83.45
115	117.45	91	95.12	87	90.75	94	90.12	90	90.75	91	95.12	88	89	83	83.45
104	102.22	94	90.75	91	92.7	94	100.21	90	91.5	93	96.12	87	90	92	95.45

## REFERENCES

- [1] Aldowish AF, Alsubaie MN, Alabdulrazzaq SS, Alsaykhan DB, Alamri AK, Alhatem LM, Algoufi JF, Alayed SS, Aljadani SS, Alashjai AM, Alamari AS. Occlusion and Its Role in the Long-Term Success of Dental Restorations: A Literature Review. *Cureus*. 2024 Nov 7;16(11):e73195. doi: 10.7759/cureus.73195. PMID: 39651022; PMCID: PMC11624512.
- [2] E.H. ANGLE, "CLASSIFICATION OF MALOCCLUSION," DENTAL COSMOS, vol. 41, no. 18, pp. 248–264, 1899, [Online]. Available: <https://sid.ir/paper/544881/en>.
- [3] Andrews LF. The six keys to normal occlusion. *Am J Orthod*. 1972 Sep;62(3):296-309. doi: 10.1016/s0002-9416(72)90268-0. PMID: 4505873.
- [4] De Angelis F, Pranno N, Franchina A, Di Carlo S, Brauner E, Ferri A, Pellegrino G, Grecchi E, Goker F, Stefanelli LV. Artificial Intelligence: A New Diagnostic Software in Dentistry: A Preliminary Performance Diagnostic Study. *Int J Environ Res Public Health*. 2022 Feb 2;19(3):1728. doi: 10.3390/ijerph19031728. PMID: 35162751; PMCID: PMC835112.
- [5] de Magalhães AA, Santos AT. Advancements in Diagnostic Methods and Imaging Technologies in Dentistry: A Literature Review of Emerging Approaches. *Journal of Clinical Medicine*. 2025; 14(4):1277. <https://doi.org/10.3390/jcm14041277>.
- [6] Shah N, Bansal N, Logani A. Recent advances in imaging technologies in dentistry. *World J Radiol*. 2014 Oct 28;6(10):794-807. doi: 10.4329/wjr.v6.i10.794. PMID: 25349663; PMCID: PMC4209425.
- [7] Abdalla-Aslan R, Yeshua T, Kabla D, Leichter I, Nadler C. An artificial intelligence system using machine-learning for automatic detection and classification of dental restorations in panoramic radiography. *Oral Surg Oral Med Oral Pathol Oral Radiol*. 2020 Nov;130(5):593-602. doi: 10.1016/j.oooo.2020.05.012. Epub 2020 Jun 3. PMID: 32646672.
- [8] Rubaba Binte Rahman, Sharia Arfin Tanim, Nazia Alfaz, Tahmid Enam Shrestha, Md Saef Ullah Miah, M.F. Mridha, A comprehensive dental dataset of six classes for deep learning based object detection study, *Data in Brief*, Volume 57, 2024, 110970, ISSN 2352-3409, <https://doi.org/10.1016/j.dib.2024.110970>. (<https://www.sciencedirect.com/science/article/pii/S2352340924009326>)
- [9] Monica Bonfanti-Gris, Angel García-Cañas, Raul Alonso-Calvo, Maria Paz Salido Rodriguez-Manzaneque, Guillermo Pradies Ramiro, Evaluation of an Artificial Intelligence web-based software to detect and classify dental structures and treatments in panoramic radiographs, *Journal of Dentistry*, Volume 126, 2022, 104301, ISSN 0300-5712, <https://doi.org/10.1016/j.jdent.2022.104301>. (<https://www.sciencedirect.com/science/article/pii/S0300571222003566>)
- [10] Datta, S., Saeed, K., Chaki, N. (2025). Identification of Caries Lesion from Colored Images. In: Analysis of Dental Imageries Towards Improved Diagnosis. Studies in Computational Intelligence, vol 1199. Springer, Singapore. (<https://doi.org/10.1007/978-981-96-3766-9-3>).
- [11] S. B. Singh, A. Laishram, K. Thongam and K. M. Singh, "Transfer Learning-Based Automated Tooth and Anomaly Classification in OPG X-ray Images," 2024 IEEE 1st International Conference on Green Industrial Electronics and Sustainable Technologies (GUEST), Imphal, India, 2024, pp. 1-6, doi: 10.1109/GUEST62955.2024.10959857.
- [12] Gupta S, Jain S. Orthopantomographic Analysis for Assessment of Mandibular Asymmetry *Journal of Indian Orthodontic Society*. 2012;46(1):33-37. doi:10.5005/jp-journals-10021-1054
- [13] Puri, Taruna. (2019). Panoramic radiographs for investigating skeletal patternsA comparative study. *International Journal of Dentistry Research*. 4. 66-78. 10.31254/dentistry.2019.4207.
- [14] Shahabi M, Ramazanzadeh BA, Mokhber N. Comparison between the external gonial angle in panoramic radiographs and lateral cephalograms of adult patients with Class I malocclusion. *J Oral Sci*. 2009 Sep;51(3):425-9. doi: 10.2334/josnusd.51.425. PMID: 19776510.
- [15] Adnan N, Khalid WB, Umer F. An artificial intelligence model for instance segmentation and tooth numbering on orthopantomograms. *Int J Comput Dent*. 2023 Nov 28;26(4):301-309. doi: 10.3290/j.ijcd.b3840535. PMID: 36705317.
- [16] Ozlu Ucan G, Gwassi OAH, Apaydin BK, Ucan B. Automated Age Estimation from OPG Images and Patient Records Using Deep Feature Extraction and Modified Genetic-Random Forest. *Diagnostics (Basel)*. 2025 Jan 29;15(3):314. doi: 10.3390/diagnostics15030314. PMID: 39941244; PMCID: PMC11817095.
- [17] Blanco, N.V., Cootes, T.F., Lindner, C., Carmona, I.T., Carreira, M.J. (2019). Fully Automatic Teeth Segmentation in Adult OPG Images. In: Vrtovec, T., Yao, J., Zheng, G., Pozo, J. (eds) Computational Methods and Clinical Applications in Musculoskeletal Imaging. MSKI 2018. Lecture Notes in Computer Science(), vol 11404. Springer, Cham. <https://doi.org/10.1007/978-3-030-11166-3-2>
- [18] R. Zannah, M. Bashar, R. B. Mushfiq, A. Chakrabarty, S. Hossain and Y.J. Jung, "Semantic Segmentation on Panoramic Dental X-Ray Images Using U-Net Architectures," in IEEE Access, vol. 12, pp. 44598-44612, 2024, doi: 10.1109/ACCESS.2024.3380027.
- [19] TRoohparvar, Sanaz & Samani, Ahmad. (2022). Intelligent System for Detecting Tooth Decay in OPG Images by Image Processing. *Frontiers in Health Informatics*. 11. 105. 10.30699/fhi.v11i1.358.
- [20] L. Bussaban, E. Boonchieng, W. Panyarak, A. Charuakkra and P. Chulamanee, "Age Group Classification From Dental Panoramic Radiographs Using Deep Learning Techniques," in IEEE Access, vol. 12, pp. 139962-139973, 2024, doi: 10.1109/ACCESS.2024.3466953.
- [21] S. Stone and P. Birkholz, "Angle Correction in Optopalatographic Tongue Distance Measurements," in IEEE Sensors Journal, vol. 17, no. 2, pp. 459-468, 15 Jan.15, 2017, doi: 10.1109/JSEN.2016.2630742.
- [22] Monica Bonfanti-Gris, Angel García-Cañas, Raul Alonso-Calvo, Maria Paz Salido Rodriguez-Manzaneque, Guillermo Pradies Ramiro, Evaluation of an Artificial Intelligence web-based software to detect and classify dental structures and treatments in panoramic radiographs, *Journal of Dentistry*, Volume 126, 2022, 104301, ISSN 0300-5712, <https://doi.org/10.1016/j.jdent.2022.104301>. (<https://www.sciencedirect.com/science/article/pii/S0300571222003566>)
- [23] Woo, Hyein & Jha, Nayansi & Kim, Yoon-Ji & Sung, Sang-Jin. (2022). Evaluating the accuracy of automated orthodontic digital setup models. *Seminars in Orthodontics*. 10.1053/j.sodo.2022.12.010.
- [24] Magkavali-Trikka P, Halazonetis DJ, Athanasiou AE. Estimation of root inclination of anterior teeth from virtual study models: accuracy of a commercial software. *Prog Orthod*. 2019 Nov 22;20(1):43. doi: 10.1186/s40510-019-0298-5. PMID: 31754914; PMCID: PMC6872682.
- [25] Al-Ubaydi, Ammar Sh., Al-Groosh, Dheaa, The Validity and Reliability of Automatic Tooth Segmentation Generated Using Artificial Intelligence, *The Scientific World Journal*, 2023, 5933003, 11 pages, 2023. <https://doi.org/10.1155/2023/5933003>.
- [26] Turosz N, Checińska K, Checiński M, Brzozowska A, Nowak Z, Sikora M. Applications of artificial intelligence in the analysis of dental panoramic radiographs: an overview of systematic reviews. *Dentomaxillofac Radiol*. 2023 Oct;52(7):20230284. doi: 10.1259/dmfr.20230284. Epub 2023 Sep 4. PMID: 37665008; PMCID: PMC10552133.
- [27] Assiri HA, Hameed MS, Alqarni A, Dawasaz AA, Arem SA, Assiri KI. Artificial Intelligence Application in a Case of Mandibular Third Molar Impaction: A Systematic Review of the Literature. *Journal of Clinical Medicine*. 2024; 13(15):4431. <https://doi.org/10.3390/jcm13154431>
- [28] Boztuna, M., Firincioglu, M., Akkaya, N. et al. Segmentation of periapical lesions with automatic deep learning on panoramic radiographs: an artificial intelligence study. *BMC Oral Health* 24, 1332 (2024). <https://doi.org/10.1186/s12903-024-05126-4>
- [29] Rubiu G, Bologna M, Cellina M, Cè M, Sala D, Pagani R, Mattavelli E, Fazzini D, Ibba S, Papa S, et al. Teeth Segmentation in Panoramic Dental X-ray Using Mask Regional Convolutional Neural Network. *Applied Sciences*. 2023; 13(13):7947. <https://doi.org/10.3390/app13137947>
- [30] Vranckx M, Van Gerven A, Willems H, Vandemeulebroucke A, Ferreira Leite A, Politis C, Jacobs R. Artificial Intelligence (AI)-Driven Molar Angulation Measurements to Predict Third Molar Eruption on Panoramic Radiographs. *International Journal of Environmental Research and Public Health*. 2020; 17(10):3716. <https://doi.org/10.3390/ijerph17103716>.
- [31] Syed A, Basim W, Muhammad AF, et al. Assessment of Age Using Orthopantomography and Artificial Intelligence: A Comparative Analysis. *medtigo J Emerg Med*. 2025;2(1):e3092214. doi:10.63096/medtigo3092214.
- [32] Chen W, Dhawan M, Liu J, Ing D, Mehta K, Tran D, Lawrence D, Ganhewa M, Cirillo N. Mapping the Use of Artificial Intelligence-Based Image Analysis for Clinical Decision-Making in Dentistry: A Scoping Review. *Clin Exp Dent Res*. 2024 Dec;10(6):e70035. doi: 10.1002/cre2.70035. PMID: 39600121; PMCID: PMC11599430.
- [33] Akdoğan S, Özçit MÜ, Tassoker M. Development of an AI-Supported Clinical Tool for Assessing Mandibular Third Molar Tooth Extraction Difficulty Using Panoramic Radiographs and YOLOv1 Sub-Models. *Diagnostics*. 2025; 15(4):462. <https://doi.org/10.3390/diagnostics15040462>
- [34] Choi, E., Lee, S., Jeong, E. et al. Artificial intelligence in positioning between mandibular third molar and inferior alveolar nerve on panoramic radiography. *Sci Rep* 12, 2456 (2022). <https://doi.org/10.1038/s41598-022-06483-2>

- [35] Pérez de Frutos, J., Holden Helland, R., Desai, S. et al. AI-Dentify: deep learning for proximal caries detection on bitewing x-ray - HUNT4 Oral Health Study. *BMC Oral Health* 24, 344 (2024). <https://doi.org/10.1186/s12903-024-04120-0>.
- [36] Qu W, Qiu Z, Lam KC, Sakaran KG, Chen H, Lin Y. Artificial intelligence-assisted identification and assessment of mandibular asymmetry on panoramic radiography. *Am J Orthod Dentofacial Orthop.* 2025 Jul;168(1):14-23.e2. doi: 10.1016/j.ajodo.2025.01.018. Epub 2025 Mar 6. PMID: 40047777.
- [37] Niha Adnan, Fahad Umer, Shahzaib Malik, Owais A. Hussain, Multi-model deep learning approach for segmentation of teeth and periapical lesions on pantomographs, Oral Surgery, Oral Medicine, Oral Pathology and Oral Radiology, Volume 138, Issue 1, 2024, Pages 196-204, ISSN 2212-4403, <https://doi.org/10.1016/j.oooo.2023.11.006>.
- [38] T. L. Koch, M. Perslev, C. Igel and S. S. Brandt, "Accurate Segmentation of Dental Panoramic Radiographs with U-NETS," 2019 IEEE 16th International Symposium on Biomedical Imaging (ISBI 2019), Venice, Italy, 2019, pp. 15-19, doi: 10.1109/ISBI.2019.8759563.
- [39] Dmitry V Tuzoff, Lyudmila N Tuzova, Michael M Bornstein, Alexey S Krasnov, Max A Kharchenko, Sergey I Nikolenko, Mikhail M Sveshnikov, Georgiy B Bednenko, Tooth detection and numbering in panoramic radiographs using convolutional neural networks, *Dentomaxillofacial Radiology*, Volume 48, Issue 4, 1 May 2019, 20180051, <https://doi.org/10.1259/dmfr.20180051>
- [40] Fahad Umer, Saqib Habib, Niha Adnan, Application of deep learning in teeth identification tasks on panoramic radiographs, *Dentomaxillofacial Radiology*, Volume 51, Issue 5, 1 July 2022, 20210504, <https://doi.org/10.1259/dmfr.20210504>
- [41] G. Jader, J. Fontineli, M. Ruiz, K. Abdalla, M. Pithon and L. Oliveira, "Deep Instance Segmentation of Teeth in Panoramic X-Ray Images," 2018 31st SIBGRAPI Conference on Graphics, Patterns and Images (SIBGRAPI), Parana, Brazil, 2018, pp. 400-407, doi: 10.1109/SIBGRAPI.2018.00058.
- [42] Muramatsu, C., Morishita, T., Takahashi, R. et al. Tooth detection and classification on panoramic radiographs for automatic dental chart filing: improved classification by multi-sized input data. *Oral Radiol* 37, 13–19 (2021). <https://doi.org/10.1007/s11282-019-00418-w>.
- [43] Ursi WJ, Almeida RR, Tavano O, Henriques JF. Assessment of mesiodistal axial inclination through panoramic radiography. *J Clin Orthod.* 1990 Mar;24(3):166-73. PMID: 2387903.
- [44] Cicek, O.; Yilmaz, H.; Demir Cicek, B. Comparison of the Mesiodistal Angulations of Canine and Molar Teeth in Different Types of Orthodontic Malocclusions: A Retrospective Study. *Diagnostics* 2023, 13, 1351. <https://doi.org/10.3390/diagnostics13071351>
- [45] Bouwens DG, Cevidan L, Ludlow JB, Phillips C. Comparison of mesiodistal root angulation with posttreatment panoramic radiographs and cone-beam computed tomography. *Am J Orthod Dentofacial Orthop.* 2011 Jan;139(1):126-32. doi: 10.1016/j.ajodo.2010.05.016. PMID: 21195286; PMCID: PMC3036614.
- [46] Rocha, Caroline Almeida, Renato Henrques, José Flores-Mir, Carlos Almeida, Marcio. (2016). Evaluation of long-term stability of mesiodistal axial inclinations of maxillary molars through panoramic radiographs in subjects treated with Pendulum appliance. *Dental Press Journal of Orthodontics.* 21, 67-74. 10.1590/2177-6709.21.1.067-074.oar.
- [47] Gautam, Utsav Shrestha, Rabindra Dhakal, Jyoti. (2025). Assessment of Mesiodistal Angulations of Mandibular Canine and Posterior Teeth using Orthopantomogram. *Orthodontic Journal of Nepal.* 14, 57-61. 10.3126/ojn.v14i1.66291.
- [48] Ananya Hazare, J.S. (2025)Evaluation of the mesiodistal angulations of maxillary and mandibular permanent canines, 1st premolar, 2nd pre molar, 1st molar and 2nd molar in relation to infraorbital and bi-gonial plane in angles class I ,class II, class III malocclusions seen in pano, *Journal of Chemical Health Risks.* Available at: <https://www.jchr.org/index.php/JCHR/article/view/5735> (Accessed: 18 December 2025).
- [49] Ansari FM, Naseem KT, Ashok A, Bavitha TK, Fawaz V, Sabu JK. Application of the OPG in the Prediction of Unfavorably Angulated Canines: An Original Study. *J Pharm Bioallied Sci.* 2023 Jul;15(Suppl 1):S180-S182. doi: 10.4103/jpbs.jpbs\_448\_22. Epub 2023 Jul 5. PMID: 37654390; PMCID: PMC4066605.
- [50] Taha Zirek, Muhammet Üsame Özic, Melek Tassoker, AI-Driven localization of all impacted teeth and prediction of winter angulation for third molars on panoramic radiographs: Clinical user interface design, *Computers in Biology and Medicine*, Volume 178, 2024, 108755, ISSN 0010-4825, <https://doi.org/10.1016/j.combiomed.2024.108755> (<https://www.sciencedirect.com/science/article/pii/S0010482524008400>)
- [51] Cicek, O.; Arslan, D. Investigation of the Mesiodistal Angulations of Maxillary Canines and Central Incisors for Missing Bilateral Maxillary Lateral Incisor. *J. Clin. Med.* 2024, 13, 2110. <https://doi.org/10.3390/jcm13072110>
- [52] Renata Rodrigues de Almeida-Pedrin, Arnaldo Pinzan, Renato Rodrigues de Almeida, Weber Ursi, Marcio Rodrigues de Almeida, Panoramic evaluation of mesiodistal axial inclinations of maxillary anterior teeth in orthodontically treated subjects, *American Journal of Orthodontics and Dentofacial Orthopedics*, Volume 130, Issue 1, 2006, Pages 56-60, ISSN 0889-5406, <https://doi.org/10.1016/j.ajodo.2006.03.001>.
- [53] Samawi SS, Burke PH. Angular distortion in the orthopantomogram. *Br J Orthod.* 1984 Apr;11(2):100-7. doi: 10.1179/bjo.11.2.100. PMID: 6587906.
- [54] Agrawal, Poonam Kapoor, D.N. Sharma, V.P. Tandon, Pradeep. (2003). Assessment of mesiodistal angulations of teeth:A panoramic radiographic study. *The Journal of Indian Orthodontic Society.* 36, 96-102. 10.1177/0974909820030206.
- [55] Shorten, C., Khoshgoftaar, T.M. A survey on Image Data Augmentation for Deep Learning. *J Big Data* 6, 60 (2019). <https://doi.org/10.1186/s40537-019-0197-0>
- [56] Perez, L., Wang, J. The effectiveness of data augmentation in image classification using deep learning. *arXiv preprint arXiv:1712.04621*, 2017. <https://arxiv.org/abs/1712.04621>
- [57] J. O'Rourke, Computational Geometry in C, Cambridge, U.K.: Cambridge University Press, 1998.
- [58] G. Strang, Linear Algebra and Its Applications, 5th ed. Boston, MA, USA: Cengage Learning, 2016.
- [59] S. Ren, K. He, R. Girshick, and J. Sun, "Faster R-CNN: Towards real-time object detection with region proposal networks," *IEEE Transactions on Pattern Analysis and Machine Intelligence*, vol. 39, no. 6, pp. 1137–1149, Jun. 2017.
- [60] K. He, G. Gkioxari, P. Dollár, and R. Girshick, "Mask R-CNN," *IEEE Transactions on Pattern Analysis and Machine Intelligence*, vol. 42, no. 2, pp. 386–397, Feb. 2020.
- [61] J. L. Devore, Probability and Statistics for Engineering and the Sciences, 9th ed. Boston, MA, USA: Cengage Learning, 2016.



**ANKITHA A NAYAK** received her B.E. degree in Information Science and Engineering from Visvesvaraya Technological University, Belagavi, and her M.Tech. in Computer Science and Engineering from NMAM Institute of Technology, Nitte. She is currently an Assistant Professor in the Department of Computer Science and Engineering at NMAM Institute of Technology, Nitte (Deemed to be University), Nitte. Her research interests include Medical Image Processing, Generative AI, Artificial Intelligence, Machine Learning, Video Processing, and Mobile Application Development. She has actively contributed to both academia and applied research, with six published patents to her credit. In addition to her teaching and research roles, she also serves as a mentor in the HPE CTY program at NMAMIT, Nitte, guiding and supporting students in technology-driven initiatives.



**DR. VENUGOPALA P. S.** completed his BE in Computer Science in the year 2002 and M.Tech from NITK in the year 2007. He obtained his PhD degree in the year 2018. His areas of interest include image and video processing, database systems, algorithms, and machine learning. He started his career as a lecturer in the year 2002 at the Dept. of CSE, NMAMIT Nitte. He had taken charge as Head of Artificial Intelligence and Data Science since September 2022. He is actively involved in academics and research activities, publishing over 15 papers in the past 5 years and three patents. He handled the responsibility of coordinator for the UG program of the CSE department for 5 years. He visited Japan under the Sakura Exchange program for 20 days in the year 2015. He was awarded the Content Guru award by Infosys for the development of course content for the industry elective subject. He is a member of the Executive Committee of the IEEE Mangalore subsection and chair-elect for the year 2025. He was awarded the Young Volunteer award by IEEE in the year 2021.

• • •



**DR. NICY THOMAS** is a final-year postgraduate in Orthodontics at A.B. Shetty Memorial Institute of Dental Sciences, Nitte (Deemed to be University), holding a BDS degree from Manipal College of Dental Sciences, MAHE, Manipal. She has expertise in orthodontic diagnosis and treatment planning, cephalometric and 3D imaging analysis, and the management of cases using fixed and removable appliances, clear aligner therapy, and interceptive orthodontics. Her professional interests include evidence-based orthodontics, digital dentistry, and interdisciplinary care, with a strong commitment to continuous learning and enhancing patient outcomes.



**DR. M. S. RAVI** is Professor and Head of Orthodontics and Dento-facial Orthopaedics and Vice Principal at A. B. Shetty Memorial Institute of Dental Sciences, Nitte (Deemed to be University), Mangalore. He earned his BDS and MDS in Orthodontics from Annamalai University, his M. Orth. R.C.S. from the Royal College of Surgeons of England and Glasgow, and a Ph.D. from Nitte University. With over three decades of academic and clinical experience, he has guided 48 postgraduate dissertations and several Ph.D. projects. His research, supported by ICMR and BRNS, focuses on orthodontic biomechanics, biomaterials, and digital dentistry. He has published 38 papers, holds one granted patent, and has multiple other patents published and applied.



**DR. ASHWINI B.**, Completed her B.E. in Information Science and Engineering in 2004 and an M.Tech and PhD from VTU. Her areas of interest include image and video processing, Computer vision, and machine learning. She is working as an Associate Professor and Head of the Department of Information Science and Engineering at NMAMIT, Nitte. Under her guidance, her UG students have received the E-YUVA BIRAC Fund for one year of 2024-25.